

# A Local Grid-Refined Numerical Groundwater Model Based on the Vertex-centred Finite-Volume Method



Yingzhi Qian<sup>a</sup>, Yan Zhu<sup>a,\*</sup>, Xiaoping Zhang<sup>b,\*</sup>, Jiming Wu<sup>c</sup>, Ming Ye<sup>d</sup>, Wei Mao<sup>a</sup>, Jingwei Wu<sup>a</sup>, Jiesheng Huang<sup>a</sup>, Jinzhong Yang<sup>a</sup>

<sup>a</sup> State Key Laboratory of Water Resources and Hydropower Engineering Science, Wuhan University, Wuhan, Hubei 430072, China

<sup>b</sup> School of Mathematics and Statistics, Wuhan University, Wuhan, Hubei, 430072, P.R. China

<sup>c</sup> Institute of Applied Physics and Computational Mathematics, Beijing 100088, P.R.China

<sup>d</sup> Department of Earth, Ocean, and Atmospheric Science, Florida State University, Tallahassee, FL 32306, USA

## ARTICLE INFO

### Keywords:

Vertex-centred finite-volume method  
Local grid refinement  
Nonmatching grids  
Groundwater simulation

## ABSTRACT

Many algorithms have been proposed to cope with groundwater numerical simulation associated with local grid refinements typically for subsurface flow driven by sources acting on diverse scales. In this context, we focus on establishing an efficient local grid refinement method with nonmatching grids for groundwater flow modelling. The new model is based on the vertex-centred finite-volume method (VCFVM). The core idea of the algorithm resting on set all unknowns on vertices, and the flux between two vertices (the numerical flux) is expressed as a function of the hydraulic heads at the vertices of the element containing the lateral surface. The total outflow of the control volume of a given vertex is expressed as the sum of numerical fluxes. Since the algorithm sets all unknowns on vertices and a control volume can be defined for each vertex, our scheme readily embeds treatment of arbitrary polygonal grids, including nonmatching grids, in the presence of local grid refinement, without additional treatment at the nonmatching nodes. Six test cases, including five assumed ones and a real-world case, were adopted to evaluate the accuracy and efficiency of the new algorithm. The hydraulic heads calculated by the new algorithm were compared with those by a widely used and tested numerical groundwater model, called MODFLOW, and the analytic solutions. The mass balance error and the CPU time were compared with those of the MODFLOW 6 model, which owns ability to cope with nonmatching grids. The results show that the new algorithm yields high accuracy and efficiency in simulating groundwater flows with local grid refinements.

## 1. Introduction

Regional groundwater simulation is important for groundwater resource management and protection. An important issue in regional groundwater simulation is local grid refinement with nonmatching grids (Wen and Gómez-Hernández, 1996), which refers to those meshes containing hanging nodes on certain edges, is required in those simulation domains with heterogeneity of subsurface formations with hydraulic conductivities spanning many scales (He and Ren, 2006; Krcmar and Sracek, 2014) or with significant hydraulic gradient variations near wells, rivers, streams, channels or ditches (Mehl and Hill, 2002). It is thus necessary to develop algorithms with ability to solve groundwater flow equation with local refined grids, so that the regional groundwater simulation, which is originally time consuming, can be done with high efficiency.

Various spatial discretization methods have been used for numerical groundwater simulations, and the three popular methods are the finite difference method (FDM) used in MODFLOW (Harbaugh et al., 2000), the finite element method (FEM) in FEFLOW (Diersch, 1998; Trefry and Muffels, 2007), and the finite volume method (FVM) in HydroGeoSphere (Brunner and Simmons, 2012). However, conventional numerical groundwater models are unideal for dealing with nonmatching grid. For example, one solution for local grid refinement in the FDM is to use variably spaced meshes and to set the widths of rows and columns to small values in the area of interest. This approach can lead to cells with large aspect ratios and unnecessary refinement in areas where such a fine resolution is not needed (Mehl and Hill, 2002).

Significant efforts have been made to overcome the limitations of conventional numerical methods in handling nonmatching grids. One method is to divide the simulation region into a parent model with

\* Corresponding Author: Yan Zhu, Phone: 86-2768775432; Fax: 86-2768776001

E-mail addresses: [zyan0701@163.com](mailto:zyan0701@163.com) (Y. Zhu), [xpzheng.math@whu.edu.cn](mailto:xpzheng.math@whu.edu.cn) (X. Zhang).

coarse grids and several child models with finer grids, the parent model provides the flux boundary or the specified head boundary for the child model (Ward et al., 1987; Remero et al., 2006). This method can lead to a significant discrepancy in the interfaces between the parent and child models since there is no feedback from the child models to the parent model (Langevin et al., 2017). Then, an iterative coupling method between the parent and child models was developed. Székely (1998) built a groundwater model based on a point-centred finite-difference framework with the parent and child grids iteratively coupled. Mehl and Hill (2002) further modified the method and applied it to MODFLOW to develop a local grid refinement model called MODFLOW-LGR. The Darcy-weighted interpolation was used to define the head boundary conditions along the interface of the child model. The accuracy of MODFLOW-LGR was proven to be better than those of one-direction coupled models and models that rely on linear interpolation along the interface. The MODFLOW-LGR model has been widely used in groundwater simulations when local grid refinement is needed (Borsi et al., 2013; Vilhelmsen et al., 2011). Dickinson et al. (2007) and Panday and Langevin (2012) further optimized the coupling method of the parent and child models to make the model suitable for refinements with nonmatching vertices. In general, the models mentioned above address the nonmatching grids by iteratively coupling the parent and child models. In addition to these iterative coupling methods, some models use additional treatments to obtain the hydraulic head or the flux in nonmatching grids and then solve the matrix equations. Among them, MODFLOW Unstructured Grid (MODFLOW-USG) (Panday, et al., 2013), which has been widely used in simulations with multiscale problems (Feinstein et al., 2016; Herckenrath et al., 2015; Krcmar and Sracek, 2014), is based on an underlying control volume finite difference (CVFD) formulation, and the flux between coarse and fine cells is calculated based on the hydraulic heads at ghost nodes and fine cell nodes. The general unstructured grid based on concepts developed for MODFLOW-USG has also been adopted in the new version of MODFLOW called MODFLOW 6 (Langevin et al., 2017). The HydroGeoSphere model, which originated from the code of FRAC3DVS (Therrien and Sudicky, 1996; Guvanasen et al., 2007), substitutes the hydraulic head at the fine nodes with the interpolation head at coarse nodes to generate a global matrix. Although the models mentioned above can be effectively implemented for nonmatching grids by solving the unified matrix equations, additional steps are required at the interface of coarse and fine grids, e.g., interpolating the hydraulic head and flux distribution at the interface.

Numerical algorithms have also been developed to address the issue of local refinement. Among them, the most widely used numerical algorithm is the multiscale method (Matouš et al., 2017). The multiscale method targets the full problem at the original resolution and attempts to directly capture the fine-scale behaviour of the solution in coarser grids (He and Ren, 2005). The multiscale method proposed by Hou and Wu (1997) was based on the FEM and called the multiscale finite element method (MFEM), and it was demonstrated to be efficient in solving scale disparity problems (Ye et al., 2004). Xie et al. (2016) improved the construction method of the basis function of the MFEM and then extended the method from 2D to 3D simulations (Xie et al., 2017). Many other multiscale models have been developed based on different spatial discretization methods, such as the FDM (Abdulle and E, 2003; Chen and Ren, 2014; Langevin et al., 2017), FVM (Jenny et al., 2003; Durlofsky et al., 2007; Hajibeygi et al., 2008; Lunati et al., 2011; Domelevo and Omnes, 2005), and mixed FVM (He and Ren, 2005; Xie et al., 2019; Chung et al., 2015; Chen and Hou, 2003; Ye et al., 2004; Fu and Chung, et al., 2019; Zhang et al., 2017). Among these models, those based on the FDM, FVM and some mixed FEM preserve the local conservation of the velocity flux. The multiscale method was originally designed for solving heterogeneity problems and has limitations in solving problems with wells. The basic functions in multiscale models were further adjusted to consider the influence caused by wells (He and Ren, 2006; Jenny and Lunati, 2009; Wolfsteiner et al., 2006;

Kramarenko et al., 2017). Additionally, multiscale models for non-matching grids were developed, and these models are more suitable for simulating groundwater flow near wells (Gao and Li, 2017; Arbogast et al., 2000; Ganis et al., 2015). These multiscale models for non-matching grids still have limitations regarding the shape of the grid. For example, these models are limited to nested grids (Ewing and Wang, 1992), triangular grids (Gao and Li, 2017), square grids (Wheeler et al., 2002; Thomas and Wheeler, 2011), and hexahedral grids (Ganis et al., 2015). Although some grid shapes, such as triangular grids and hexahedral grids, can flexibly deal with problems requiring local grid refinements, a numerical model without limitation on grid shape would be more general and flexible. Additionally, many of the models mentioned above were designed to simulate groundwater flow in a confined aquifer (Xie et al., 2019; Chen and Ren, 2014; Gao and Li, 2017; Kramarenko et al., 2017; Zhang et al., 2017), but their applicability in unconfined aquifer problems, which are often nonlinear, has not been assessed.

In this paper, a new algorithm for solving groundwater flow equation with nonmatching grid based on the vertex-centred finite-volume method is developed. The algorithm is designed for anisotropic diffusion problems based on arbitrary polygonal grids. There are three kinds of unknowns involved, including vertex-centred, edge-midpoint and cell-centred unknowns. The vertex-centred unknowns are primary and associated with finite volume equations. The edge-midpoint and cell-centred unknowns are treated as auxiliary unknowns and are interpolated based on the primary unknowns; therefore, the final scheme is a pure vertex-centred scheme. The main novelty of the presented algorithm is that it is applicable for not only arbitrary polygonal grids but also nonmatching grids, which makes local refinements more flexible when compared to standard methods or those Hybrid FE methods (Matthai et al., 2005; Matthai et al., 2007). The new groundwater model (hereinafter referred to as the VCFVM) is constructed based on the above algorithm since the groundwater problem is a special case type of diffusion problem. Six test cases, including a heterogeneous anisotropic aquifer, a single pumping well in confined and unconfined aquifers, multiple pumping wells in a confined aquifer, two parallel canals in an unconfined aquifer with nonpoint sink/source items and a real-world test case with multiple pumping wells at field scale, were designed to evaluate the accuracy and efficiency of the new algorithm. The major contribution of this work is that it provides a new alternative to solve the confined and unconfined groundwater flow equations with arbitrary polygonal grids, including nonmatching grids, using a unified approach, regardless to the shape or form of the grids, and the method strictly conserves the local mass balance. The paper is organized as follows. The numerical algorithm of the VCFVM is introduced in Section 2. Five virtual test cases and a real-world test case used to verify the accuracy and efficiency of the VCFVM are shown in Section 3. The results of the test cases are shown in Section 4, and the simulation results are compared with those of widely used models (MODFLOW or MODFLOW 6) and the analytical solution to demonstrate the accuracy and efficiency of the VCFVM. Conclusions are given in Section 5.

## 2. VCFVM numerical algorithm

### 2.1. VCFVM for confined aquifers

Let  $\Omega \subset \mathbb{R}^2$  be the two-dimensional solution domain, and use  $\Omega^T = \Omega \times (0, T]$  to denote the spatiotemporal region of interest.  $\Omega^0 = \Omega \times \{0\}$  denotes the initial region.  $\Gamma_D^T = \Gamma_D \times (0, T]$  denotes a first-type boundary (Dirichlet boundary), and  $\Gamma_N^T = \Gamma_N \times (0, T]$  denotes a second-type boundary (Neumann boundary). Moreover, let  $\mathbf{x} = (x, y)$  be a spatial point in  $\Omega$  and  $(\mathbf{x}, t)$  be a spatiotemporal point in  $\Omega^T$ , in this case, a groundwater problem involving a confined aquifer can be mathematically described as

$$\nabla \cdot (\mathbf{K} \nabla h) = \mu_e \frac{\partial h}{\partial t} + f(\mathbf{x}, t), \quad (\mathbf{x}, t) \in \Omega^T \quad (1a)$$

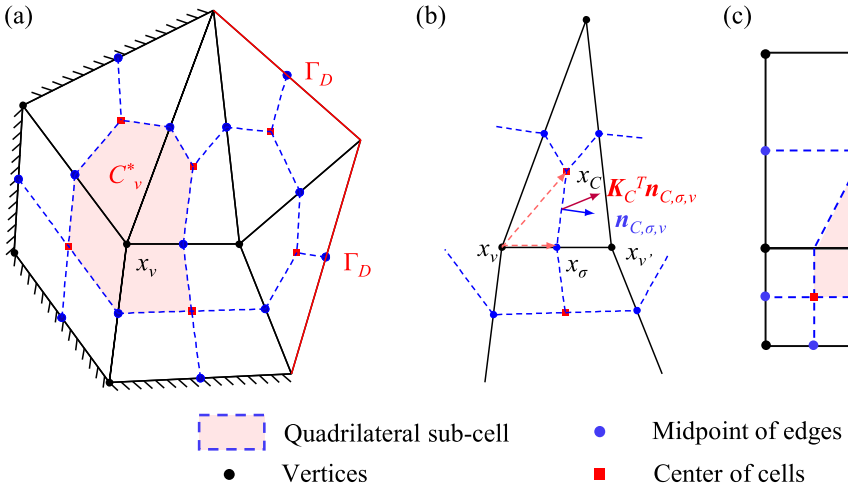


**Fig. 1.** Sketch maps of (a) the primary mesh (solid line) and the dual mesh (dashed line) for normal vertices, (b) notations for the construction of the numerical flux, (c) the primary mesh (solid line) and the dual mesh (dashed line) for nonmatching vertices. Note:  $x_v$ ,  $(x_v)$ ,  $x_\sigma$  and  $x_C$  denote the specified vertex, midpoint of the edge and cell centre in  $\Omega$ ;  $\Gamma_D$  is the boundary of  $\Omega$ ;  $K_C$  is the constant restriction of transmissivity  $K$  on cell  $C$ ;  $n_{C,\sigma,v}$  refers to the unit vectors normal to the dual edge  $x_\sigma x_C$  outwards to the dual cell associated with the vertex  $x_v$ .

$$h(\mathbf{x}, t) = g_0(\mathbf{x}), (\mathbf{x}, t) \in \Omega^0$$

(1a)

$$h(\mathbf{x}, t) = g_1(\mathbf{x}, t), (\mathbf{x}, t) \in \Gamma_D^T$$

(1b)

$$\mathbf{K} \nabla h(\mathbf{x}, t) \cdot \mathbf{n}(\mathbf{x}) = g_2(\mathbf{x}, t), (\mathbf{x}, t) \in \Gamma_N^T$$

(1c)

where  $h$  is the hydraulic head ([L]);  $\mu_e = \mu_s M$  is the elastic release coefficient of the confined aquifer ([·]) based on specific storativity  $\mu_s$  ([L<sup>-1</sup>]) and the thickness of aquifer  $M$  ([L]);  $\nabla$  is the gradient operator, which is defined by  $\nabla h = \left( \frac{\partial h}{\partial x}, \frac{\partial h}{\partial y} \right)^T$ ;  $g_0$ ,  $g_1$  and  $g_2$  are the specified initial value, Dirichlet value and Neumann value of the problem, respectively; and  $\mathbf{n}(\mathbf{x})$  denotes the unit normal vector outward to  $\Omega$  at the Neumann boundary. Moreover,  $\mathbf{K} = K_s M$  is the transmissivity of the confined aquifer, and

$$\mathbf{K}_s = \begin{pmatrix} K_{xx} & K_{xy} \\ K_{yx} & K_{yy} \end{pmatrix} \quad (2)$$

denotes the saturated hydraulic conductivity tensor.  $K_{xx}$  and  $K_{yy}$  are the saturated hydraulic conductivities in the  $x$  and  $y$  directions, respectively, [LT<sup>-1</sup>], and  $K_{xy}$  and  $K_{yx}$  are the cross-conductivity terms, [LT<sup>-1</sup>]. Thus,

$$\nabla \cdot (\mathbf{K} \nabla h) = \frac{\partial}{\partial x} \left( MK_{xx} \frac{\partial h}{\partial x} + MK_{xy} \frac{\partial h}{\partial y} \right) + \frac{\partial}{\partial y} \left( MK_{yx} \frac{\partial h}{\partial x} + MK_{yy} \frac{\partial h}{\partial y} \right) \quad (3)$$

and  $f$  is the source/sink term defined by,

$$f = P - E - \sum_{i=1}^{N_w} Q_i \delta(\mathbf{x} - \mathbf{x}_i) \quad (4)$$

where  $P = P(\mathbf{x}, t)$  denotes the amount of precipitation infiltration that leads to groundwater recharge ([LT<sup>-1</sup>]);  $E = E(\mathbf{x}, t)$  is the evapotranspiration of groundwater ([LT<sup>-1</sup>]);  $Q_i$  represents the pumping capacity of a pumping well located at  $(x_i, y_i)$ ;  $N_w$  is the number of pumping wells; and  $\delta$  is the Dirac delta function, which satisfies the following conditions:

$$\delta(\mathbf{x}) = \begin{cases} 0, & \mathbf{x} \neq 0, \\ \infty, & \mathbf{x} = 0, \end{cases} \text{ and } \int_{\mathbb{R}^2} \delta(\mathbf{x}) d\mathbf{x} = 1 \quad (5)$$

The physical meaning of Eq. (1a) reflects the mass conservation relation of groundwater flow in an aquifer and represents a water balance relation per unit volume and unit time in the aquifer under the Darcy flow conditions. That is, the difference between a mass of water flowing into and out of a unit volume aquifer per unit time (the left side of Eq. (1a)) is equal to the amount of water released (or stored) elastically in the unit volume aquifer at the same time (the right side of Eq.

(1a)).

## 2.2. Spatial discretization

The space domain  $\Omega$  is partitioned into several nonoverlapping polygonal cells that form so-called primary meshes for spatial discretization, shown as the meshes with solid line segments in Fig. 1(a).  $\Gamma_D$  is the boundary of  $\Omega$ , and  $x_v$  is a vertex of  $\Omega$ . The cell centre is defined as the geometric centre, and the corresponding coordinates are a simple average of the cell vertices. Each primary cell is further partitioned into several quadrilateral sub-cells by connecting the cell centre with the midpoint of edges, as shown by the dashed line segments in Fig. 1(a). All sub-cells sharing the same vertex in the primary mesh form a polygonal cell in the dual mesh, as shown in the highlighted part of Fig. 1(a), denoted as  $C_v^*$ , which is the control volume of the corresponding vertex (e.g., vertex  $x_v$ ). In regards to those vertices lie on the nonmatching edge (denoted as nonmatching vertex here in and after), their control volumes are formed by connecting the centre of the neighbour cells with the midpoint of edges that sharing the vertex, which is similar to those normal vertices, shown as the vertex  $x_v$  and the corresponding control volume  $C_v^*$  in Fig. 1(c). Since the control volumes of all vertices (including nonmatching vertices) can be formed using a unified approach, there is no difference in the spatial and temporal discretization schemes among normal and nonmatching vertices, and the spatial and temporal discretization schemes for the nonmatching vertices will not be illustrated separately in the following sections.

For the primary and dual meshes, we introduce two types of unknowns: the primary unknowns and the auxiliary unknowns. The primary unknowns are defined at the vertices of the primary mesh in  $\Omega$  or on  $\partial\Omega \setminus \Gamma_D$  and are shown as black solid circles in Fig. 1(a). Each primary unknown is associated with a finite volume (FV) equation. The auxiliary unknowns are defined at the cell centres and edge midpoints of the primary mesh and are denoted by red solid squares and blue solid circles in Fig. 1(a), respectively. These auxiliary unknowns do not have corresponding FV equations, and they are evaluated based on the primary unknowns or, if necessary, Dirichlet boundary data, which will be discussed in detail later in the paper.

After forming the control volume of each vertex (including the nonmatching vertices), the numerical flux outwards a specified control volume via a specified dual edge is constructed. Let  $x_v$  and  $x_{v'}$  be two interior vertices of the primary mesh sharing edge  $\sigma$  for primary cell  $C$ , as shown in Fig. 1(b). Let  $x_\sigma$ ,  $x_C$ ,  $e_C$  and  $K_C$  denote the midpoint of the edge  $\sigma$ , the centre of  $C$ , the set of edges of  $C$  and the constant restriction of  $\mathbf{K}$  on  $C$ , respectively.  $\mathbf{N}_{C,\sigma,v}$  (resp.  $\mathbf{n}_{C,\sigma,v}$ ) refers to the unit vector normal to the dual edge  $x_\sigma x_C$  outward to the dual cell associated with the vertex  $x_v$  (resp.  $x_{v'}$ ). Obviously,  $\mathbf{n}_{C,\sigma,v} = -\mathbf{n}_{C,\sigma,v'}$ . In addition, let  $\epsilon_v$  (resp.  $M_v$ ) be

the set of primary edges (resp. primary cells) sharing  $\mathbf{x}_v$ .

According to Darcy's law, the flow velocity  $\mathbf{v}$  in the primary cell  $C$  can be defined by

$$\mathbf{v} = -\mathbf{K}_c \nabla h \quad (6)$$

Since only the component of velocity normal to the dual edge contributes to the outflow, the outflow of the control volume crossing the dual edge  $\mathbf{x}_\sigma \mathbf{x}_C$  can be defined by

$$F_{C,\sigma,v} = |\mathbf{x}_\sigma \mathbf{x}_C| \mathbf{v} \cdot \mathbf{n}_{C,\sigma,v} = -\nabla h \cdot (\mathbf{x}_\sigma \mathbf{x}_C | \mathbf{K}_C^T \mathbf{n}_{C,\sigma,v}) \quad (7)$$

where  $|\mathbf{x}_\sigma \mathbf{x}_C|$  denotes the length of the edge  $\mathbf{x}_\sigma \mathbf{x}_C$ . The vector  $|\mathbf{x}_\sigma \mathbf{x}_C| \mathbf{K}_C^T \mathbf{n}_{C,\sigma,v}$  can be decomposed as a linear combination of two vectors  $\mathbf{x}_\sigma \mathbf{x}_C$  and  $\mathbf{x}_v \mathbf{x}_\sigma$ :

$$|\mathbf{x}_\sigma \mathbf{x}_C| \mathbf{K}_C^T \mathbf{n}_{C,\sigma,v} = \alpha_{C,\sigma,v} (\mathbf{x}_C - \mathbf{x}_v) + \beta_{C,\sigma,v} (\mathbf{x}_\sigma - \mathbf{x}_v) \quad (8)$$

where  $\alpha_{C,\sigma,v}$  and  $\beta_{C,\sigma,v}$  are the two combination coefficients. These coefficients are expressed as

$$\alpha_{C,\sigma,v} = \frac{|\mathbf{x}_\sigma \mathbf{x}_C| \mathbf{n}_{C,\sigma,v}^T \mathbf{K}_C^T \mathbf{R} (\mathbf{x}_\sigma - \mathbf{x}_v)}{(\mathbf{x}_C - \mathbf{x}_v)^T \mathbf{R} (\mathbf{x}_\sigma - \mathbf{x}_v)} \quad (9a)$$

$$\beta_{C,\sigma,v} = \frac{|\mathbf{x}_\sigma \mathbf{x}_C| \mathbf{n}_{C,\sigma,v}^T \mathbf{K}_C^T \mathbf{R} (\mathbf{x}_C - \mathbf{x}_v)}{(\mathbf{x}_\sigma - \mathbf{x}_v)^T \mathbf{R} (\mathbf{x}_C - \mathbf{x}_v)} \quad (9b)$$

where  $\mathbf{R}$  is a rotation matrix that makes a vector rotate 90 degrees counterclockwise, i.e.,

$$\mathbf{R} = \begin{pmatrix} 0 & -1 \\ 1 & 0 \end{pmatrix} \quad (10)$$

Substituting Eq. (8) into Eq. (7) leads to

$$F_{C,\sigma,v} = -\nabla h \cdot [\alpha_{C,\sigma,v} (\mathbf{x}_C - \mathbf{x}_v) + \beta_{C,\sigma,v} (\mathbf{x}_\sigma - \mathbf{x}_v)] \cong \alpha_{C,\sigma,v} (h_v - h_C) + \beta_{C,\sigma,v} (h_v - h_\sigma) \quad (11)$$

Similarly, based on the following vector splitting,

$$|\mathbf{x}_\sigma \mathbf{x}_C| \mathbf{K}_C^T \mathbf{n}_{C,\sigma,v'} = \alpha_{C,\sigma,v'} (\mathbf{x}_C - \mathbf{x}_{v'}) + \beta_{C,\sigma,v'} (\mathbf{x}_\sigma - \mathbf{x}_{v'}) \quad (12)$$

the following equation is obtained

$$F_{C,\sigma,v'} \cong \alpha_{C,\sigma,v'} (h_{v'} - h_C) + \beta_{C,\sigma,v'} (h_{v'} - h_\sigma) \quad (13)$$

where,

$$\alpha_{C,\sigma,v'} = \frac{|\mathbf{x}_\sigma \mathbf{x}_C| \mathbf{n}_{C,\sigma,v'}^T \mathbf{K}_C^T \mathbf{R} (\mathbf{x}_\sigma - \mathbf{x}_{v'})}{(\mathbf{x}_C - \mathbf{x}_{v'})^T \mathbf{R} (\mathbf{x}_\sigma - \mathbf{x}_{v'})} \quad (14a)$$

$$\beta_{C,\sigma,v'} = \frac{|\mathbf{x}_\sigma \mathbf{x}_C| \mathbf{n}_{C,\sigma,v'}^T \mathbf{K}_C^T \mathbf{R} (\mathbf{x}_C - \mathbf{x}_{v'})}{(\mathbf{x}_\sigma - \mathbf{x}_{v'})^T \mathbf{R} (\mathbf{x}_C - \mathbf{x}_{v'})} \quad (14b)$$

For the control volume  $C_v^*$  associated with the specified vertex  $\mathbf{x}_v$ , the total outflow  $F_v$  is the sum of the outflows crossing the dual edges of  $C_v^*$ . Then the left-hand side of Eq. (1a) can be approximated by

$$F_v = \sum_{C \in M_v} \sum_{\sigma \in \mathcal{E}_C \cap \mathcal{E}_v} F_{C,\sigma,v} \quad (15)$$

and therefore, the finite volume equation associated with a specific vertex  $\mathbf{x}_v$  of  $\Omega \cap \Gamma_D$  can be constructed as follows,

$$F_v = \int_{C_v^*} \mu_e \frac{\partial h}{\partial t} dx + \int_{C_v^*} f dx \approx \mu_e |C_v^*| \frac{\partial h_v}{\partial t} + |C_v^*| f(\mathbf{x}_v) \quad (16)$$

where  $|C_v^*|$  denotes the area of the dual cell  $C_v^*$ . The matrix form of Eq. (16) is,

$$\bar{\mathbf{A}}\mathbf{h} = \mu_e \Lambda \frac{\partial h}{\partial t} + \Lambda f \quad (17)$$

where  $\bar{\mathbf{A}}$  is a coefficient matrix. The value of element in the  $m$ -th row and  $n$ -th column of  $\bar{\mathbf{A}}$  (denoted as  $\bar{A}_{m,n}$ ) is given in Section 2.4 after introducing the interpolation approach of auxiliary unknowns;  $\mathbf{h}$  is a vector related to  $h_v$ ;  $f$  is a vector related to  $f(\mathbf{x}_v)$ ; and  $\Lambda$  is a diagonal matrix with  $|C_v^*|$  diagonal elements.

In regards of the accuracy order of the proposed spatial discretization, it was investigated by simulating scenarios using different kinds of challenging meshes with different resolutions, as shown in Section 3.1, and the simulation results indicate that the VCFVM has a second-order spatial accuracy. The details can be found in Section 3.1 and Section 4.1.

### 2.3. Interpolation of auxiliary unknowns and analysis of local conservation

In order to obtain a fully vertex-centred finite volume scheme, the auxiliary unknowns need to be interpolated based on the primary unknowns. In the proposed scheme, since the auxiliary unknowns are defined at the centres and edge midpoints of the primary cells, they can be easily interpolated based on the vertex unknowns. Let  $\mathbf{x}_\sigma$  be the midpoint of  $\sigma$  with endpoints  $\mathbf{x}_v$  and  $\mathbf{x}_{v'}$ .  $\mathbf{x}_C$  is the geometric centre of primary cell  $C$ . Then, for the auxiliary unknowns defined at  $\mathbf{x}_\sigma$  and  $\mathbf{x}_C$ , elimination can be performed based on the following interpolation strategies:

$$h_\sigma = \frac{h_v + h_{v'}}{2} \quad (18)$$

and

$$h_C = \frac{1}{n_C} \sum_{\mathbf{x}_v \in v_C} h_v \quad (19)$$

where  $v_C$  denotes the set of vertices in cell  $C$ ;  $n_C$  denotes the number of vertices in cell  $C$ . It should be noted that in Eq. (18), the influence of other vertices is ignored (e.g., in Fig. 1(b),  $h_\sigma$  is assumed to be only related to  $h_v$  and  $h_{v'}$ , which are the two endpoints of the corresponding edge  $\sigma$ , while the influences of other vertices in the cell  $C$  are ignored). In other words, Eq. (18) and Eq. (19) assume the unknown changes linearly in a given cell, and this may introduce nonnegligible error in cases that the size of the given cell is too large to ignore the nonlinearity of unknown within the cell. However, since the interpolation approach is not the focus of this research and linear interpolation methods are widely used in numerical models, such as the method used in MODFLOW-USG to obtain the hydraulic head at a ghost node (Panday et al., 2013), a linear approach is also adopted here to obtain the pressure head at the midpoint. It should be noted that fine grids are needed in those regions where unknown changes highly nonlinearly, to avoid unacceptable errors introduced by the linear interpolation scheme adopted, as what we do in the test cases shown in Section 3.

At the end of this subsection, we investigate the local conservation of numerical flux, which is the basis of the finite volume method. The medium properties (e.g.,  $\mathbf{K}$ ) are defined over the elements in the proposed method, thus the  $\mathbf{K}_C^T$  of Eq. (9) is equal to that of Eq. (14). And for the meshes used in those scenarios involving heterogeneous layers, faults, pinchouts and fractures, the edges of the primary cells should be aligned with the interface to have exact definition of the medium properties in the spatial domain (Manzoor et al., 2021), and for the scenarios involving pumping wells or other point sources, vertices are required to be aligned with those points. Consequently, we have following lemma.

**Lemma 1.** If primary  $C$  is a star-shaped cell whose cell centre is  $\mathbf{x}_C$ , then for the coefficients in the numerical flux equation defined in Eq. (9) and Eq. (14), we have

$$\alpha_{C,\sigma,v} + \beta_{C,\sigma,v} = \alpha_{C,\sigma,v'} + \beta_{C,\sigma,v'} \quad (20)$$

$$\alpha_{C,\sigma,v} + \alpha_{C,\sigma,v'} = 0 \quad (21)$$

**Proof.** . Since  $C$  is a star-shaped cell with respect to  $\mathbf{x}_C$ , we have

$$(\mathbf{x}_C - \mathbf{x}_v)^T \mathbf{R}(\mathbf{x}_\sigma - \mathbf{x}_v) = -(\mathbf{x}_\sigma - \mathbf{x}_v)^T \mathbf{R}(\mathbf{x}_C - \mathbf{x}_v) = -|\mathbf{x}_\sigma \mathbf{x}_C| d_{C,\sigma,v},$$

where  $d_{C,\sigma,v}$  denotes the distance from vertex  $\mathbf{x}_v$  to the dual edge  $\mathbf{x}_\sigma \mathbf{x}_C$ . Then we deduce from Eq. (9) and Eq. (14) that

$$\alpha_{C,\sigma,v} + \beta_{C,\sigma,v} = \frac{|\mathbf{x}_\sigma \mathbf{x}_C| \mathbf{n}_{C,\sigma,v}^T \mathbf{K}_C^T \mathbf{R}(\mathbf{x}_\sigma - \mathbf{x}_C)}{(\mathbf{x}_C - \mathbf{x}_v)^T \mathbf{R}(\mathbf{x}_\sigma - \mathbf{x}_v)} = \frac{|\mathbf{x}_\sigma \mathbf{x}_C| \mathbf{n}_{C,\sigma,v}^T \mathbf{K}_C^T \mathbf{n}_{C,\sigma,v}}{d_{C,\sigma,v}},$$

where we have used the identity  $\mathbf{R}(\mathbf{x}_\sigma - \mathbf{x}_C) = -|\mathbf{x}_\sigma \mathbf{x}_C| \mathbf{n}_{C,\sigma,v}$ . And similarly, we have

$$\alpha_{C,\sigma,v'} + \beta_{C,\sigma,v'} = \frac{|\mathbf{x}_\sigma \mathbf{x}_C| \mathbf{n}_{C,\sigma,v'}^T \mathbf{K}_C^T \mathbf{n}_{C,\sigma,v'}}{d_{C,\sigma,v'}},$$

where  $d_{C,\sigma,v'}$  denotes the distance from vertex  $\mathbf{x}_v'$  to the dual edge  $\mathbf{x}_\sigma \mathbf{x}_C$ . Since  $\mathbf{x}_\sigma$  is the midpoint of primary edge, we have  $d_{C,\sigma,v} = d_{C,\sigma,v'}$ . Recalling that  $\mathbf{n}_{C,\sigma,v} = -\mathbf{n}_{C,\sigma,v'}$ , and  $\mathbf{K}_C$  is positive definite, we obtain Eq. (20). As for (21), we have

$$(\mathbf{x}_C - \mathbf{x}_v)^T \mathbf{R}(\mathbf{x}_\sigma - \mathbf{x}_v) = -(\mathbf{x}_C - \mathbf{x}_v')^T \mathbf{R}(\mathbf{x}_\sigma - \mathbf{x}_v')$$

and consequently, we have

$$\begin{aligned} \alpha_{C,\sigma,v} + \alpha_{C,\sigma,v'} &= \frac{|\mathbf{x}_\sigma \mathbf{x}_C| \mathbf{n}_{C,\sigma,v}^T \mathbf{K}_C^T \mathbf{R}(\mathbf{x}_\sigma - \mathbf{x}_v)}{(\mathbf{x}_C - \mathbf{x}_v)^T \mathbf{R}(\mathbf{x}_\sigma - \mathbf{x}_v)} + \frac{|\mathbf{x}_\sigma \mathbf{x}_C| \mathbf{n}_{C,\sigma,v'}^T \mathbf{K}_C^T \mathbf{R}(\mathbf{x}_\sigma - \mathbf{x}_v')}{(\mathbf{x}_C - \mathbf{x}_v')^T \mathbf{R}(\mathbf{x}_\sigma - \mathbf{x}_v')} \\ &= \frac{|\mathbf{x}_\sigma \mathbf{x}_C| \mathbf{n}_{C,\sigma,v}^T \mathbf{K}_C^T \mathbf{R}(2\mathbf{x}_\sigma - \mathbf{x}_v - \mathbf{x}_v')}{(\mathbf{x}_C - \mathbf{x}_v)^T \mathbf{R}(\mathbf{x}_\sigma - \mathbf{x}_v)} = 0. \end{aligned}$$

The properties shown in Eq. (20) and Eq. (21) are crucial for the derivation of the local conservation of numerical flux, and deducing from them, we have the following lemma.

**Lemma 2.** If primary  $C$  is a star-shaped cell whose cell centre is  $\mathbf{x}_C$ , then for the numerical fluxes defined in Eq. (11) and Eq. (13), we have

$$F_{C,\sigma,v} + F_{C,\sigma,v'} = 0 \quad (22)$$

**Proof.** According to the definitions of  $F_{C,\sigma,v}$  and  $F_{C,\sigma,v'}$  in Eq. (11) and Eq. (13), we have

$$F_{C,\sigma,v} + F_{C,\sigma,v'} = (\alpha_{C,\sigma,v} + \beta_{C,\sigma,v})(h_v - h_\sigma) + (\alpha_{C,\sigma,v'} + \beta_{C,\sigma,v'})(h_{v'} - h_\sigma).$$

Recalling Eq. (20) and Eq. (21), we have

$$\begin{aligned} F_{C,\sigma,v} + F_{C,\sigma,v'} &= (\alpha_{C,\sigma,v} + \beta_{C,\sigma,v})(h_v + h_{v'}) - (\beta_{C,\sigma,v} + \beta_{C,\sigma,v'})h_\sigma \\ &= (2\alpha_{C,\sigma,v} + \beta_{C,\sigma,v} - \beta_{C,\sigma,v'})h_\sigma = 0, \end{aligned}$$

where we have used the identity  $h_\sigma = \frac{h_v + h_{v'}}{2}$ .

**Lemma 2** demonstrated that the numerical fluxes are continuous crossing the dual edge of control volume for both normal grids and nonmatching grids. It should be pointed out that the flux continuity across the grid cell's face is not considered in the VCFVM. However, in many practical problems, especially in the cases that there are jumps in medium properties, the flux continuity across interfaces that separate changes in medium properties is a concerned issue, and its importance has been verified by comparison for two-phase flow between standard control volume finite element (CVFE) and control volume distributed multipoint flux approximation (CVD-MPFA) in the literatures (Edwards, 2006a; Edwards, 2006b), in which it has been proved that the CVD-MPFA method with flux-continuity across crucial interfaces where the medium properties jump yields highly resolved solutions. It is worth mentioning that the reference of Wu (2017) proposed a post-processing

technique to make a vertex-centred finite volume scheme satisfy the flux continuity across the grid cell's faces, which can also be applicable to our approach. It is an interesting topic to further discuss how to make the vertex-centred scheme assure the flux continuity across the grid cell's faces, which will also be studied in the future.

#### 2.4. Extending the VCFVM to unconfined aquifers

For an unconfined aquifer, the groundwater problem can be expressed by Eq. (1), except Eq. (1a) must be slightly modified. In this case, the transmissivity  $\mathbf{K}$  has the form,

$$K(h) = K_s \cdot h \quad (23)$$

and  $K_s$  is the saturated hydraulic conductivity tensor defined by Eq. (2). Notably, the transmissivity tensor is dependent on the hydraulic head  $h$ , which makes Eq. (1a) a nonlinear partial differential equation,

$$\frac{\partial}{\partial x} \left( K_{xx} h \frac{\partial h}{\partial x} + K_{xy} h \frac{\partial h}{\partial y} \right) + \frac{\partial}{\partial y} \left( K_{yx} h \frac{\partial h}{\partial x} + K_{yy} h \frac{\partial h}{\partial y} \right) = \mu_d \frac{\partial h}{\partial t} + f \quad (24)$$

or in a more compact form,

$$\nabla \cdot (\mathbf{K}(h) \nabla h) = \mu_d \frac{\partial h}{\partial t} + f \quad (25)$$

where  $\mu_d$  is the specified yield of the unconfined aquifer (unitless).

The difference of VCFVM between unconfined aquifer and confined aquifer mainly exists in the construction of numerical flux. To be specific, since the transmissivity  $K(h)$  depends on  $h$  in an unconfined aquifer, the corresponding combination coefficients defined in Eq. (9a) and Eq. (9b) should be modified to

$$\alpha_{C,\sigma,v}(h) = \frac{|\mathbf{x}_\sigma \mathbf{x}_C| \mathbf{n}_{C,\sigma,v}^T \mathbf{K}_C^T(\mathbf{h}) \mathbf{R}(\mathbf{x}_\sigma - \mathbf{x}_v)}{(\mathbf{x}_C - \mathbf{x}_v)^T \mathbf{R}(\mathbf{x}_\sigma - \mathbf{x}_v)} \quad (26a)$$

$$\beta_{C,\sigma,v}(h) = \frac{|\mathbf{x}_\sigma \mathbf{x}_C| \mathbf{n}_{C,\sigma,v}^T \mathbf{K}_C^T(\mathbf{h}) \mathbf{R}(\mathbf{x}_C - \mathbf{x}_v)}{(\mathbf{x}_\sigma - \mathbf{x}_v)^T \mathbf{R}(\mathbf{x}_C - \mathbf{x}_v)} \quad (26b)$$

and similar modifications are made for  $\alpha_{C,\sigma,v'}(h)$  and  $\beta_{C,\sigma,v'}(h)$ . Obviously, Lemma 1 and 2 for the confined aquifer still stand up for the unconfined aquifer, and the matrix equation after spatial discretization has the same form of Eq. (17).

#### 2.5. Temporal discretization and the discrete equations

Considering the interpolation approach introduced in Section 2.3, the value of the element in the  $m$ -th row and  $n$ -th column of matrix  $\bar{\mathbf{A}}$ , denoted as  $\bar{A}_{m,n}$ , could be expressed as Eq. (27), and an illustrative example is given in Appendix A to show the value of each element in the discrete equation associated to a given mesh which contains non-matching vertices.

$$\bar{A}_{m,n} = \begin{cases} \sum_{C \in M_m} \sum_{\sigma \in \mathcal{E}_C \cap \mathcal{E}_m} \left( \alpha_{C,\sigma,m} + \frac{\beta_{C,\sigma,m}}{2} - \frac{\alpha_{C,\sigma,m}}{N_A} \right) m = n \\ - \sum_{C \in M_m \cap M_n} \sum_{\sigma \in \mathcal{E}_m \cap \mathcal{E}_n} \frac{\beta_{C,\sigma,m}}{2} - \sum_{C \in M_m \cap M_n} \sum_{\sigma \in \mathcal{E}_C \cap \mathcal{E}_m} \frac{\alpha_{C,\sigma,m}}{N_A} m \neq n \end{cases} \quad (27)$$

To develop the final numerical scheme to solve Eq. (1), temporal discretization is needed based on Eq. (27). We partition the time interval  $[0, T]$  as

$$0 = t_0 < t_1 < \dots < t_N = T,$$

and both Back Euler method and Crank-Nicolson method are provided here for temporal discretization, therefore, the corresponding accuracy orders in temporal domain are first-order and second-order, respectively.

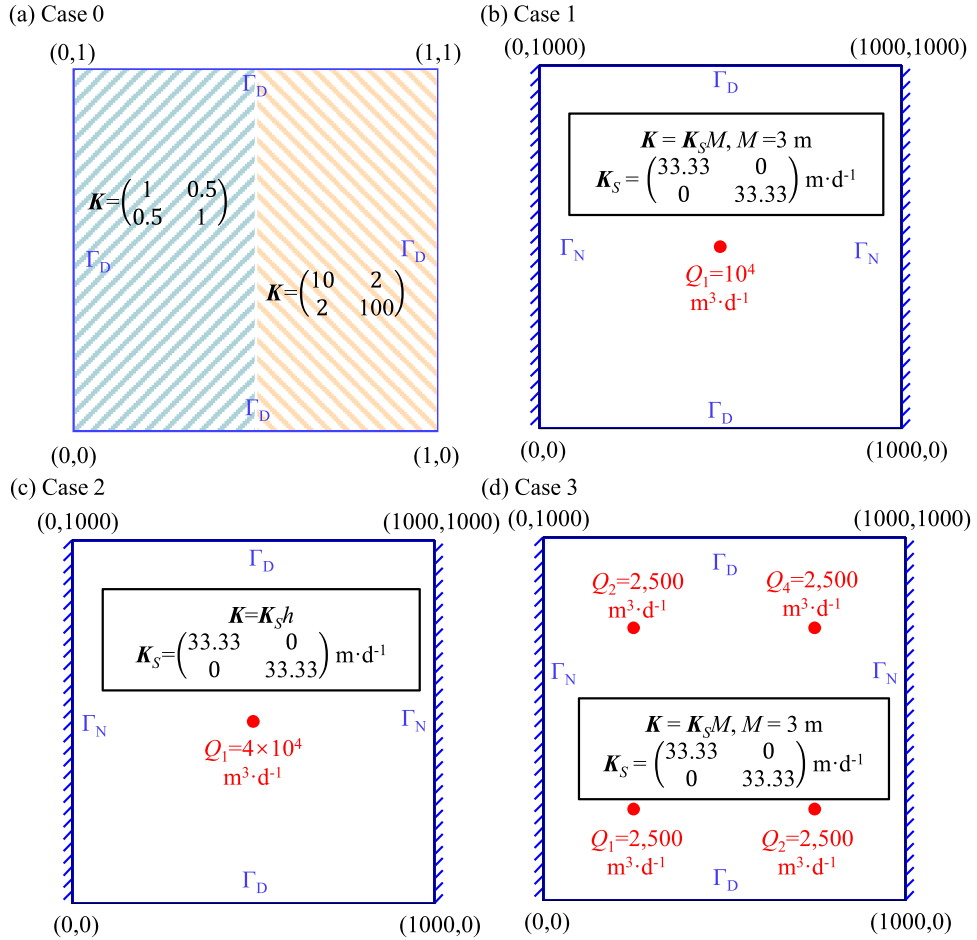


**Fig. 2.** Test settings for (a) case 0, (b) case 1, (c) case 2, and (d) case 3.

For Back Euler method, Eq. (17) is discretized as

$$\bar{\mathbf{A}}\mathbf{h}^{n+1} = \mu_e \Lambda \frac{\mathbf{h}^{n+1} - \mathbf{h}^n}{\tau} + \Lambda f, \quad n = 0, \dots, N-1 \quad (28)$$

where the superscript  $n$  denotes the  $n$ -th time point and  $\tau$  denotes the corresponding time step size. Equivalently, this relation can also be expressed as follows,

$$\mathbf{A}\mathbf{h}^{n+1} = \mathbf{b}, \quad n = 0, \dots, N-1 \quad (29)$$

where

$$\mathbf{A} = \tau^{-1} \mu_e \Lambda - \bar{\mathbf{A}}, \quad \mathbf{b} = \tau^{-1} \mu_e \Lambda \mathbf{h}^n - \Lambda f \quad (30)$$

and the element in the  $m$ -th row and  $n$ -th column of  $\mathbf{A}$  (denoted as  $\mathbf{A}_{m,n}$ ) could be obtained according to the following equation,

$$\mathbf{A}_{m,n} = \begin{cases} \frac{|C_m| \mu_e}{\tau} - \sum_{C \in M_m} \sum_{\sigma \in \varepsilon_C \cap \varepsilon_m} \left( \alpha_{C,\sigma,m} + \frac{\beta_{C,\sigma,m}}{2} - \frac{\alpha_{C,\sigma,m}}{N_A} \right) m = n \\ \sum_{C \in M_m \cap M_n} \sum_{\sigma \in \varepsilon_m \cap \varepsilon_n} \frac{\beta_{C,\sigma,m}}{2} + \sum_{C \in M_m \cap M_n} \sum_{\sigma \in \varepsilon_C \cap \varepsilon_m} \frac{\alpha_{C,\sigma,m}}{N_A} m \neq n \end{cases} \quad (31)$$

For Crank-Nicolson method, Eq. (17) is discretized as

$$\bar{\mathbf{A}} \frac{\mathbf{h}^{n+1} + \mathbf{h}^n}{2} = \mu_e \Lambda \frac{\mathbf{h}^{n+1} - \mathbf{h}^n}{\tau} + \Lambda f, \quad n = 0, \dots, N-1 \quad (32)$$

Equivalently, it can be expressed as Eq. (29), where

$$\mathbf{A} = \tau^{-1} \mu_d \Lambda - \frac{1}{2} \bar{\mathbf{A}}, \quad \mathbf{b} = \tau^{-1} \mu_d \Lambda \mathbf{h}^n - \Lambda f + \frac{1}{2} \bar{\mathbf{A}} \mathbf{h}^n \quad (33)$$

and the value of  $\mathbf{A}_{m,n}$  could be obtained according to the following equation

$$\mathbf{A}_{m,n} = \begin{cases} \frac{|C_m| \mu_e}{\tau} - \frac{1}{2} \sum_{C \in M_m} \sum_{\sigma \in \varepsilon_C \cap \varepsilon_m} \left( \alpha_{C,\sigma,m} + \frac{\beta_{C,\sigma,m}}{2} - \frac{\alpha_{C,\sigma,m}}{N_A} \right) m = n \\ \sum_{C \in M_m \cap M_n} \sum_{\sigma \in \varepsilon_m \cap \varepsilon_n} \frac{\beta_{C,\sigma,m}}{2} + \sum_{C \in M_m \cap M_n} \sum_{\sigma \in \varepsilon_C \cap \varepsilon_m} \frac{\alpha_{C,\sigma,m}}{N_A} m \neq n \end{cases} \quad (34)$$

To solve the equation defined in Eq. (29), Krylov subspace methods (Saad., 2003), including Generalized Minimum Residual (GMRES) and Bi-Conjugate Gradient Stabilized (BiCGSTAB), are adopted in the VCFVM.

### 3. Test cases and model evaluation indices

To evaluate the accuracy and efficiency of the VCFVM, six test cases were implemented, and the simulation results were compared with the numerical results of MODFLOW (or MODFLOW 6) and the analytical solution. The VCFVM was run in Ubuntu 18.04 with GCC 7.3.0. The details of each case are introduced below.

#### 3.1. Case 0: Piecewise bilinear field

We adopt this case (Edwards and Zheng, 2010) to evaluate the actual performance of the VCFVM in simulating cases involving highly heterogeneous aquifer with full tensor transmissivity, and also to investigate the spatial accuracy order of the VCFVM. A piecewise bilinear field is defined over the unitless spatial domain  $\Omega = [0, 1] \times [0, 1]$ , and involves a permeability field with a discontinuity at  $x = 0.5$ . The left

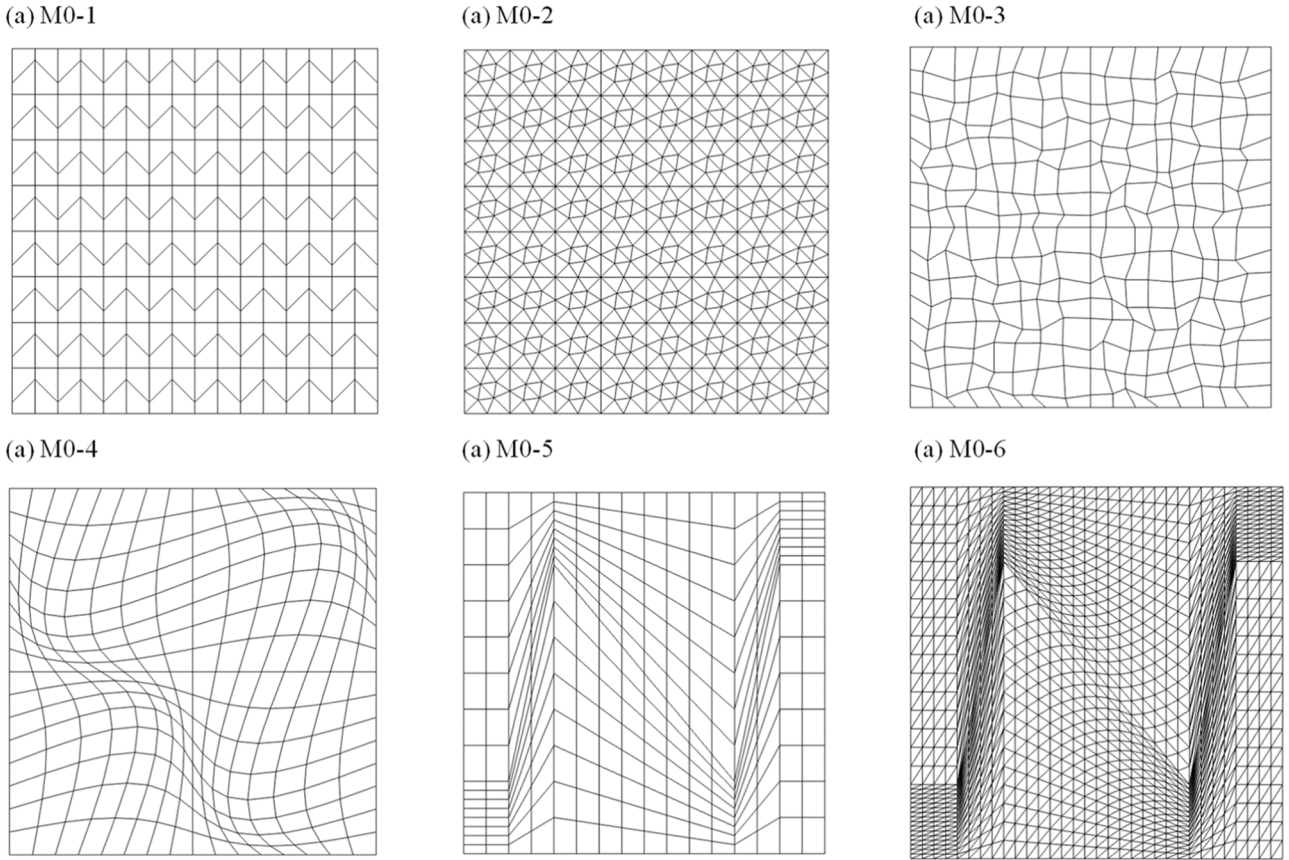


**Fig. 3.** Different mesh schemes used in case 0: (a) Quadrangle trapezoidal mesh, (b) Triangle classic, (c) Quadrangle random, (d) Quadrangle Shashkov, (e) Quadrangle Kershaw and (f) Triangle Kershaw meshes.

transmissivity  $\mathbf{K}_L$  and the right one  $\mathbf{K}_R$  are defined as

$$\mathbf{K}_L = \begin{pmatrix} 1 & 0.5 \\ 0.5 & 1 \end{pmatrix}, \quad \mathbf{K}_R = \begin{pmatrix} 10 & 2 \\ 2 & 100 \end{pmatrix}$$

The exact pressure field is defined by

$$h = \begin{cases} 10 + 20xy, & x \leq \frac{1}{2} \\ 10.75 - 1.5x + 9y + 2xy, & x > \frac{1}{2} \end{cases} \quad (36)$$

All boundaries of the spatial domain  $\Omega$  are defined as Dirichlet

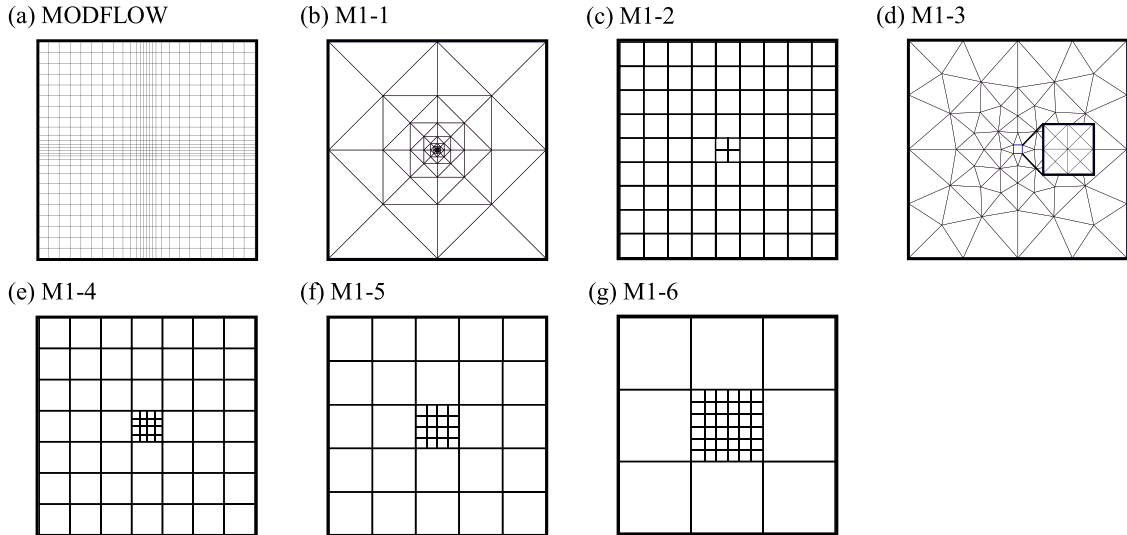


**Fig. 4.** Different mesh schemes used in case 1: (a) the mesh for MODFLOW, and the different mesh schemes used by the VCFVM as indicated by (b) the normal triangle mesh (M1-1), (c) the quadrilateral local refined grid with a 1:2 refine ratio (M1-2), (d) the triangle local refined grid (M1-3), (e) the quadrilateral local refined grid with a 1:4 refinement ratio (M1-4), (f) the quadrilateral local refined grid with a 1:4 refinement ratio and coarser grid (M1-5), and (g) the quadrilateral local refined grid with a 1:6 refinement ratio (M1-6).

**Table 1**

Basic information of different mesh schemes of case 1, case 3 and case 5.

Case number	Mesh code	Number of vertices	Number of cells
Case 1	MODFLOW	729	676
	M1-1	108	206
	M1-2	105	84
	M1-3	77	160
	M1-4	85	64
	M1-5	57	40
Case 3	M1-6	61	44
	MODFLOW	1089	1024
	M3-1	286	582
	M3-2	205	160
Case 5	M3-3	190	322
	VCFVM	7781	7247
	MODFLOW 6	7781	7247

boundary conditions with  $g_1(x, t)$  equal to the defined exact pressure on boundaries. All these test settings are shown in Fig. 2(a).

We employ six kinds of meshes (denoted as M0-1 to M0-6), including Quadrangle trapezoidal, Triangle classic, Quadrangle random, Quadrangle Shashkov, Quadrangle Kershaw and Triangle Kershaw meshes, to simulate this case. The sketch map of each mesh is shown in Fig. 3. Moreover, each kind of mesh is simulated with 5 resolution levels, in order to investigate the spatial accuracy order of the VCFVM. Besides Case 0, a more challenging test case (denoted as Case A0) involving medium coefficients with large anisotropy ratio at different orientation is provided in Appendix B to show the robustness of VCFVM in those scenarios.

### 3.2. Case 1: Single pumping well in a confined aquifer

This case is designed to evaluate the performance of the VCFVM for problems involving confined aquifers, the performance of the VCFVM in dealing with LGR meshes, and the adaptability of the VCFVM to different local mesh refinement ratios. The study domain has a size of  $1,000^2$  m, i.e.,  $\Omega = [0, 1000] \times [0, 1000]$ , and the confined aquifer is homogeneous and isotropic. The thickness ( $M$ ) of the aquifer is 3 m, the elastic release coefficient  $\mu_e$  is 0.001, and the saturated hydraulic conductivity  $K_{xx} = K_{yy}$  is  $33.33 \text{ m}\cdot\text{d}^{-1}$ , while the cross-conductivity terms  $K_{xy}$  and  $K_{yx}$  are not considered. The left and right boundaries are non-flux boundaries, i.e.,  $g_2(x, y, t) \equiv 0$  m, and the top and bottom boundaries are constant-head boundaries with a value of 100 m, i.e.,  $g_1(x, y, t) \equiv 100$  m. The initial hydraulic head is assumed to be constant, i.e.,  $g_0(x, y) \equiv 100$  m. A pumping well is located at the centre of  $\Omega$  with a pumping rate of  $10^4 \text{ m}^3/\text{d}$ , i.e.,  $N_w = 1$ ,  $x_1 = (500, 500)$ , and  $Q_1 = 10^4 \text{ m}^3\cdot\text{d}^{-1}$ , additionally, the effects of precipitation infiltration and evapotranspiration are not considered, i.e.,  $P = E \equiv 0 \text{ m}\cdot\text{d}^{-1}$  in Eq. (4). The well pumps water from the first day to the 20th day, i.e.,  $T = 20$  days. The backwards Euler method defined in Eq. (28) is used for temporal discretization. All these test settings are shown in Fig. 2(b).

The mesh used by MODFLOW is a variable grid, as shown in Fig. 4(a). However, considering the influence of the pumping wells, it is preferable to use a LGR mesh, which is fine near the well and coarse away from the

well, to reduce the computational cost and improve the computational speed without sacrificing accuracy. The proposed VCFVM is suitable for arbitrary polygonal meshes, which makes the local refinement of the mesh flexible. To demonstrate the performance of the VCFVM in dealing with LGR meshes, three LGR mesh schemes are used in this case, as shown in Fig. 4(b)-(d) and denoted as M1-1, M1-2 and M1-3. It should be noted that the mesh schemes shown in Fig. 4(c) and Fig. 4(d) involve nonmatching vertices. The basic information for each mesh scheme mentioned above is given in Table 1.

To test the adaptability of the VCFVM to different local grid refinement ratios, four LGR meshes with different refinement ratios were considered, as shown in Fig. 4 and denoted as M1-2, M1-4, M1-5 and M1-6. The results were compared to those of MODFLOW 6, which is also skilled in dealing with nonmatching grids, using the same meshes. It should be noted that, although the refinement ratio of M1-4 equals that of M1-5, the corresponding coarse grid sizes are different. Moreover, convex angles exist in the control volume formed by the vertices at the interface of coarse and fine cells in the LGR meshes discussed above, which may not be allowed in some models. The basic information for each mesh scheme mentioned above is given in Table 1.

### 3.3. Case 2: Single pumping well in an unconfined aquifer

This case is designed to test the accuracy of the VCFVM in an unconfined aquifer. A square homogeneous isotropic unconfined aquifer with a side length of 1000 m and aquifer thickness  $M$  equal to 100 m was established. The specific yield of the unconfined aquifer  $\mu_d$  was 0.1, and the saturated hydraulic conductivities  $K_x$  and  $K_y$  were  $33.33 \text{ m}\cdot\text{d}^{-1}$ . The left and right boundaries were specified as non-flux boundaries, i.e.,  $g_2 \equiv 0 \text{ m}\cdot\text{d}^{-1}$ , and the top and bottom boundaries were constant-head boundaries with  $g_1 \equiv 90$  m. The initial hydraulic head was constant at  $g_0 = 90$  m. A pumping well was located in the centre of the region, and the pumping rate was  $Q_1 = 4000 \text{ m}^3\cdot\text{d}^{-1}$ . The pumping lasted for 20 days. The Crank-Nicolson method defined in Eq. (32) was adopted for temporal discretization. The problem settings are illustrated in Fig. 2(c).

This case was also explored with MODFLOW with the meshes shown in Fig. 3(a) and the VCFVM with the three mesh schemes shown in Fig. 4(b)-(d) and denoted as M2-1, M2-2 and M2-3 for case 2, respectively.

### 3.4. Case 3: Multiple pumping wells in a confined aquifer

This case is designed to demonstrate the accuracy of the VCFVM in a case with multiple wells. The mesh geometry, aquifer properties and initial and boundary conditions of the aquifer in this case are the same as those in case 1. In this case, there are four ( $N_w = 4$ ) pumping wells located at the following locations:  $x_1 = (250, 250)$ ,  $x_2 = (750, 250)$ ,  $x_3 = (750, 750)$  and  $x_4 = (250, 750)$ . The pumping rate of each well is  $Q_i = 2500 \text{ m}^3\cdot\text{d}^{-1}$ , where  $i = 1, \dots, 4$ , and pumping lasts for 20 days, i.e.,  $T = 20$  days. The backwards Euler method defined in Eq. (28) is used for temporal discretization. These test settings are shown in Fig. 2(d).

This case was explored using MODFLOW with the mesh shown in Fig. 5(a) and using the VCFVM with the three mesh schemes shown in

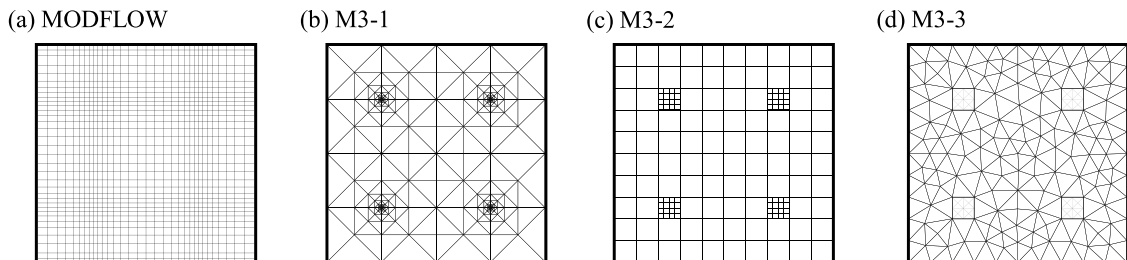


**Fig. 5.** The mesh schemes used in case 3, (a) the mesh for MODFLOW, and the three mesh schemes used for the VCFVM as indicated by (b) the normal triangle mesh (M3-1), (c) the quadrilateral mesh with local refined grids (M3-2), and (d) the triangle mesh with local refined grids (M3-3).

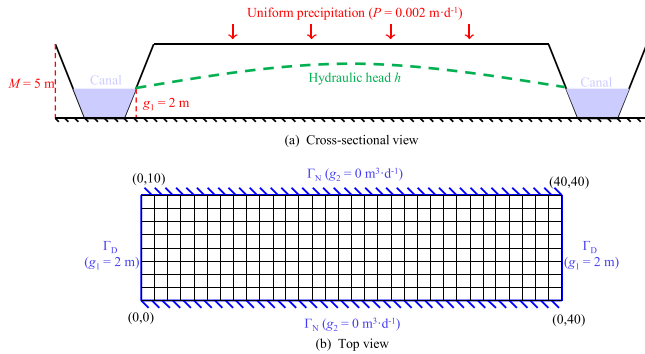


**Fig. 6.** Problem settings for case 4.

**Fig. 5(b)-(d)**, which are a normal triangular mesh, a triangular mesh with local refined grids and a quadrilateral mesh with local refined grids, denoted as M3-1, M3-2 and M3-3, respectively. The basic information for each mesh scheme is given in **Table 1**.

### 3.5. Case 4: Two parallel canals

This case is designed to test the accuracy of the VCFVM in simulating groundwater movement with a nonpoint source/sink term, as defined in Eq. (4). The unconfined aquifer is homogeneous, isotropic, and bounded by two parallel canals at a distance of 40 m on each side. The saturated hydraulic conductivity and the specific yield are  $K_{xx} = 0.5 \text{ m}\cdot\text{d}^{-1}$  and  $\mu_d = 0.1$ , respectively. The uniform precipitation rate  $P = 0.002 \text{ m}\cdot\text{d}^{-1}$  is considered without evapotranspiration or pumping. The water surface height in the two canals is 2 m (based on the bottom boundary). The change in the groundwater level in the unconfined aquifer within 100 days is calculated. A cross-sectional view of the unconfined aquifer is shown in **Fig. 6(a)**. The top and bottom sides are set as nonflux boundaries, i.e.,  $g_2 = 0 \text{ m}^3\cdot\text{d}^{-1}$ , and the left and right sides are set as constant-head boundaries, i.e.,  $g_1 = 2 \text{ m}$ . A uniform rectangular mesh is used by both MODFLOW and VCFVM in this case, as shown in **Fig. 6(b)**.

### 3.6. Case 5: Application of VCFVM to a real-world groundwater simulation

To assess the accuracy and efficiency of the VCFVM in scenarios with

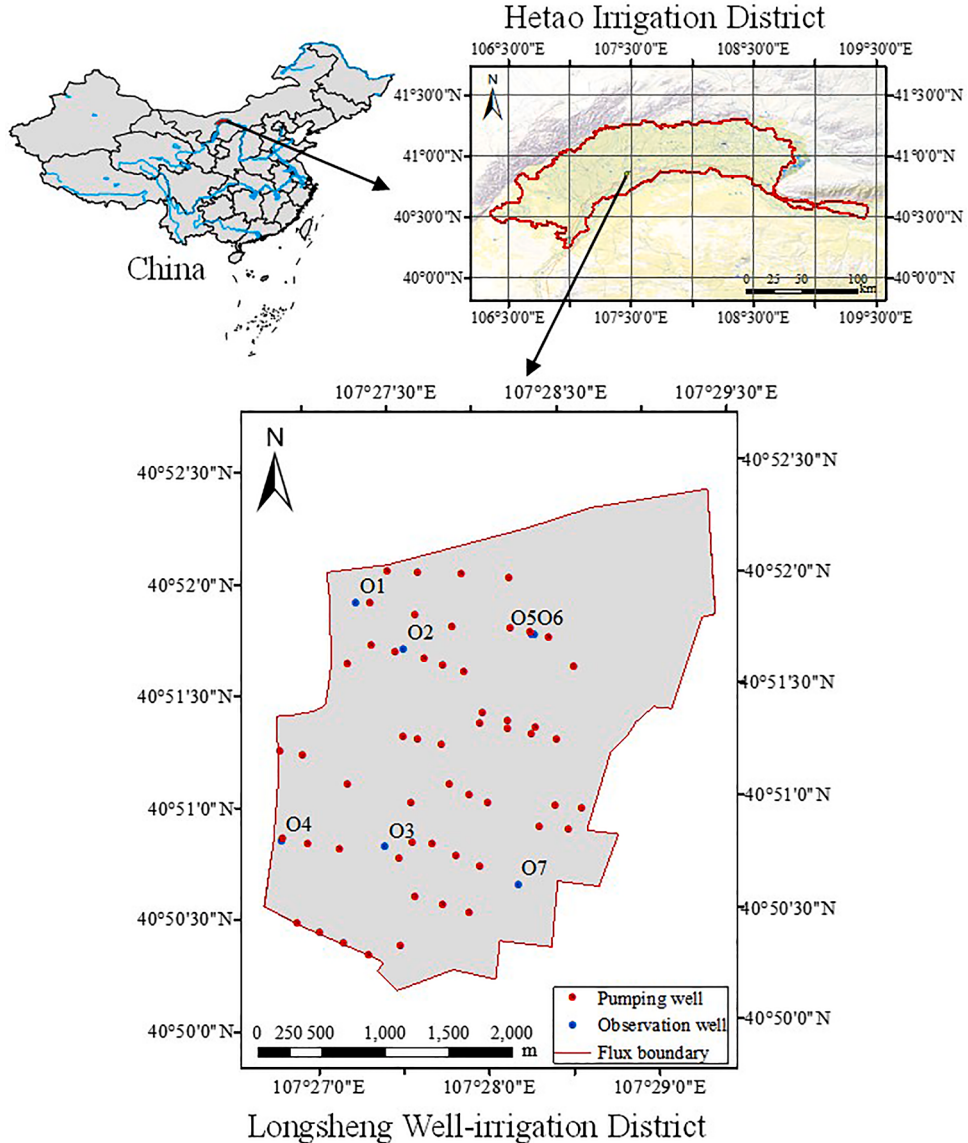


**Fig. 7.** Geographic location of the Longsheng well irrigation district and the locations of pumping wells and observation wells.

**Table 2**

The input data of case 5.

Month	5	6	7	8	9	10	11
P (mm)	4.2	12.9	32.1	49.1	58.3	6.1	4.1
E' (mm)	184.6	194.0	160.3	143.6	109.3	119.8	58.6
K (-)	0.438	0.478	0.516	0.567	0.6	0.592	0.594
R <sub>b</sub> (m/d)	0.016	0.016	0.017	0.017	0.045	0.015	0.048

Note: P is the precipitation rate; E' is the pan evaporation rate; K is a conversion coefficient and is the ratio of natural water evaporation to pan evaporation; R<sub>b</sub> is the recharge flux on the boundary.

complex conditions, the model was applied to simulate the groundwater flow in Longsheng Irrigation District (107°26'46"-107°29'20" E, 40°50'13"-40°52'19" N), a well-irrigation district of Hetao Irrigation District, located in Inner Mongolia, China, as shown in Fig. 7. The area of Longsheng Irrigation District is 9.06 km<sup>2</sup>, including 5.29 km<sup>2</sup> of farmland. There are 54 pumping wells in the district, and the irrigation water in the plant growth period (from May to September) and the leaching water in the nongrowth period (November) come from these pumping wells. There are seven observation wells established in the district (indicated as O1 to O7) to observe the groundwater level. The locations of pumping wells and observation wells are shown in Fig. 7. In this district, the irrigation quota in the plant growth period is 294 mm, and quota for autumn leaching is 180 mm. The shallow aquifer in this area is dominated by clayey sand, silty sand and clay, and the lower part is dominated by silty fine sand and medium fine sand. The average aquifer thickness is 136 m.

For numerical simulation, the aquifer was divided into one unconfined layer in the vertical direction with a thickness of 136 m. The specific yield of the aquifer was set as 0.04, and the horizontal hydraulic conductivity was set as 9.26 m/d according to previous references (Yang et al., 2021). There are lateral recharges from the surrounding areas, and the recharge fluxes (R<sub>b</sub>) in each stress period were validated based on observed values, as given in Table 2. The simulation temporal domain lasted from May to November 2018. The stress period was 30 d, and the time step was 1 d. The point sources and sinks in the district mainly come from pumping wells. The corresponding total pumping flux in each stress period was obtained according to the irrigation quota or leaching quota, and the total flux was averaged over 54 wells. The calculated pumping flux of each well was 261 m<sup>3</sup>/d from May to September, and 622 m<sup>3</sup>/d in November. The nonpoint sources and sinks in the district included precipitation, irrigation and phreatic evaporation. The precipitation rate (P) and pan evaporation rate in 2018 were from the data recorded by the Linhe weather station, as given in Table 2. The precipitation recharge coefficient was set as 0.1, and the phreatic evaporation was calculated by Eq. (37):

$$E = K \cdot T \cdot E' \quad (37)$$

where E and E' are the phreatic evaporation rate and pan evaporation rate, respectively, mm; K is a conversion coefficient and is the ratio of natural water evaporation to pan evaporation, which varies in different months; T is the phreatic evaporation coefficient, which is the ratio of phreatic evaporation at different groundwater table depths to the natural water evaporation. The values of K and T were set according to the results of experiments at the Bayan Gaole test station and Jiefangzha Shahao canal (Yang et al., 2021), respectively, as given in Table 2 and Table 3. The critical groundwater table depth of phreatic evaporation was 4 m. Irrigation water was applied only on farmland. The calculated irrigation recharge rate was 8.63 × 10<sup>-5</sup> m/d from May to September

and 3.73 × 10<sup>-4</sup> m/d in November.

MODFLOW 6 was also used here for comparison with the VCFVM. The mesh in this case for MODFLOW 6 was generated by gridgen.exe (Lien et al., 2015), which was provided on the website of MODFLOW 6. The simulation region was divided into unified rectangular cells with a length of 35.5 m and a width of 39.6 m. Then, the cells near the pumping wells were locally refined with a refinement ratio of 2, and the smoothing function provided by gridgen.exe was run. The mesh in this case for the VCFVM was generated based on a self-written program to transfer the mesh generated by gridgen.exe into the format required by the VCFVM. The basic information for the meshes used in MODFLOW 6 and the VCFVM is given in Table 1. It should be noted that the numbers of vertices and cells were the same for MODFLOW 6 and the VCFVM, since the VCFVM mesh was generated based on the MODFLOW 6 mesh.

### 3.7. Model evaluation indices

To quantify the errors of VCFVM compared to the exact solutions in case 0, the relative error E<sub>2</sub> (Zhang et al., 2017) is used, which is defined as

$$E_2 = \sqrt{\frac{\sum_{i=1}^n |C_i^*| (f_i - y_i)^2}{\sum_{i=1}^n |C_i^*| y_i^2}} \quad (38)$$

where f<sub>i</sub> is the simulated values of the VCFVM; y<sub>i</sub> is the values of benchmark; and n is the sample size. The rate of convergence R<sub>a</sub> (Zhang et al., 2017) is used to judge the accuracy of algorithm, which is obtained by the following formula

$$R_a = \frac{\log[E_2(s_2)/E_2(s_1)]}{\log(s_2/s_1)} \quad (39)$$

where s<sub>1</sub> and s<sub>2</sub> are the element sizes of two meshes with successive resolutions.

For other cases, to quantify the discrepancies between the simulated results of the VCFVM and MODFLOW/MODFLOW 6 or the analytic solution, two evaluation indices, including the mean absolute error (MAE) and the relative root mean square error (RRMSE), are used as follows:

$$MAE = \frac{1}{n} \sum_{i=1}^n |f_i - y_i| \quad (40)$$

$$RRMSE = \sqrt{\frac{\sum_{i=1}^n (f_i - y_i)^2}{n \cdot (\frac{1}{n} \sum_{i=1}^n y_i)^2}} \quad (41)$$

For case 0, the evaluation indices were calculated based on the values of all the vertices, while for other cases, the evaluation indices

**Table 4**

Specific information of observation points for different cases.

Observation point number	Case 1 and 2		Case 3	
	x	y	x	y
1	250	250	125	125
2	500	250	250	125
3	750	250	375	125
4	250	500	125	250
5	750	500	375	250
6	250	750	125	375
7	500	750	250	375
8	750	750	375	375

**Table 3**

Phreatic evaporation coefficient at different groundwater table depths in case 5.

Groundwater table depth (m)	0	0.5	1.0	1.5	2.1	2.5	3.0	3.5	4.0
T (-)	1	0.462	0.263	0.164	0.097	0.071	0.048	0.0221	0

**Table 5**  
The errors and convergence orders of the VCFVM in case 0.

Meshes	$E_2$	Refined levels				
		1	2	3	4	5
M0-1	1.675E-	1.004E-	5.716E-	1.341E-	9.126E-	
	14	12	13	13	13	
M0-2	2.865E-	6.931E-	1.714E-	4.273E-	1.068E-	
	02	03	03	04	04	
M0-3	$R_\alpha$ /	2.047	2.016	2.004	2.001	
	$E_2$	1.999E-	9.403E-	2.462E-	6.881E-	1.793E-
M0-4	02	03	03	04	04	
	$R_\alpha$ /	1.174	1.848	1.951	1.902	
M0-5	$E_2$	2.376E-	6.874E-	2.015E-	5.428E-	1.393E-
	02	03	03	04	04	
M0-6	$R_\alpha$ /	2.134	1.849	1.913	1.967	
	$E_2$	5.678E-	2.541E-	9.434E03	2.822E-	7.049E-
M0-7	02	02	03	04	04	
	$R_\alpha$ /	1.369	1.538	1.803	2.035	
M0-8	$E_2$	7.599E-	3.575E-	1.415E-	4.502E-	7.159E-
	02	02	02	03	04	
$R_\alpha$ /		1.284	1.438	1.711	2.698	

were calculated based on the values at several selected observation points, which were distributed around the whole area but not close to wells or boundaries. The coordinates of the observation points for different cases are given in Table 4.

In addition to the evaluation indices mentioned above, the total CPU time and the water balance error ( $E_B$ ) are used as evaluation indices to evaluate the efficiency of the VCFVM in problems involving LGR meshes.  $E_B$  is defined as follows:

$$E_B = \left| \frac{\sum_{i=0}^{N_v} \mu |C_i^*| (h_i^{T_F} - h_i^0) + \sum_{j=0}^{N_B} Q_j}{\max(\sum_{i=0}^{N_v} \mu |C_i^*| |h_i^{T_F} - h_i^0|, \sum_{j=0}^{N_B} |Q_j|)} \right| \times 100\% \quad (42)$$

where  $N_v$  and  $N_B$  are the numbers of vertices and boundaries,

respectively;  $\mu$  refers to  $\mu_d$  (for a confined aquifer) or  $\mu_e$  (for an unconfined aquifer);  $Q$  is the total flux at the boundary (outflow is positive and inflow is negative); the subscripts  $i$  and  $j$  refer to the codes of vertices and boundaries, respectively; and the superscripts 0 and  $T_F$  refer to the initial and final time levels, respectively.

#### 4. Results and discussion

##### 4.1. Accuracy of the VCFVM in conventional groundwater simulations

The accuracy of the VCFVM for problems involving highly heterogeneous aquifer with full tensor transmissivity is demonstrated based on the case 0, and the accuracy of the VCFVM for problems with confined aquifers is demonstrated based on cases 1 and 3 by using different kinds of meshes, and the accuracy of the VCFVM for problems with unconfined aquifers and nonpoint source/sink terms is demonstrated based on test cases 2 and 4, respectively.

The relative errors  $E_2$  of the VCFVM in case 0 on each mesh and refined level compared to the exact value are calculated and given in Table 5. It can be found that the VCFVM yields the exact solution within 12 decimal places on M0-1 for all refined levels. And for other more challenging meshes (e.g., M0-2 to M0-6), the accuracy of the VCFVM increase with the increasement of the refined level, and can yield the exact solution within 4 decimal places when the refined levels reach 5. The high accuracy of the VCFVM in case 0 demonstrates the accuracy of the VCFVM in simulating cases involving highly heterogeneous aquifer with full tensor transmissivity. Moreover, the rates of convergence  $R_\alpha$  are calculated for all families of meshes used in case 0, except for M0-1. The  $R_\alpha$  for M0-1 is not calculated since the accuracy of the VCFVM on M0-1 is already close to the machine precision, so that  $R_\alpha$  is meaningless for this mesh. The  $R_\alpha$  given in Table 5 indicate the VCFVM has a second-order spatial accuracy, as introduced in Section 2.2.

The hydraulic heads at 20 d in the simulation domain, and in the observation profile, located at  $x=500$  m, calculated by MODFLOW and

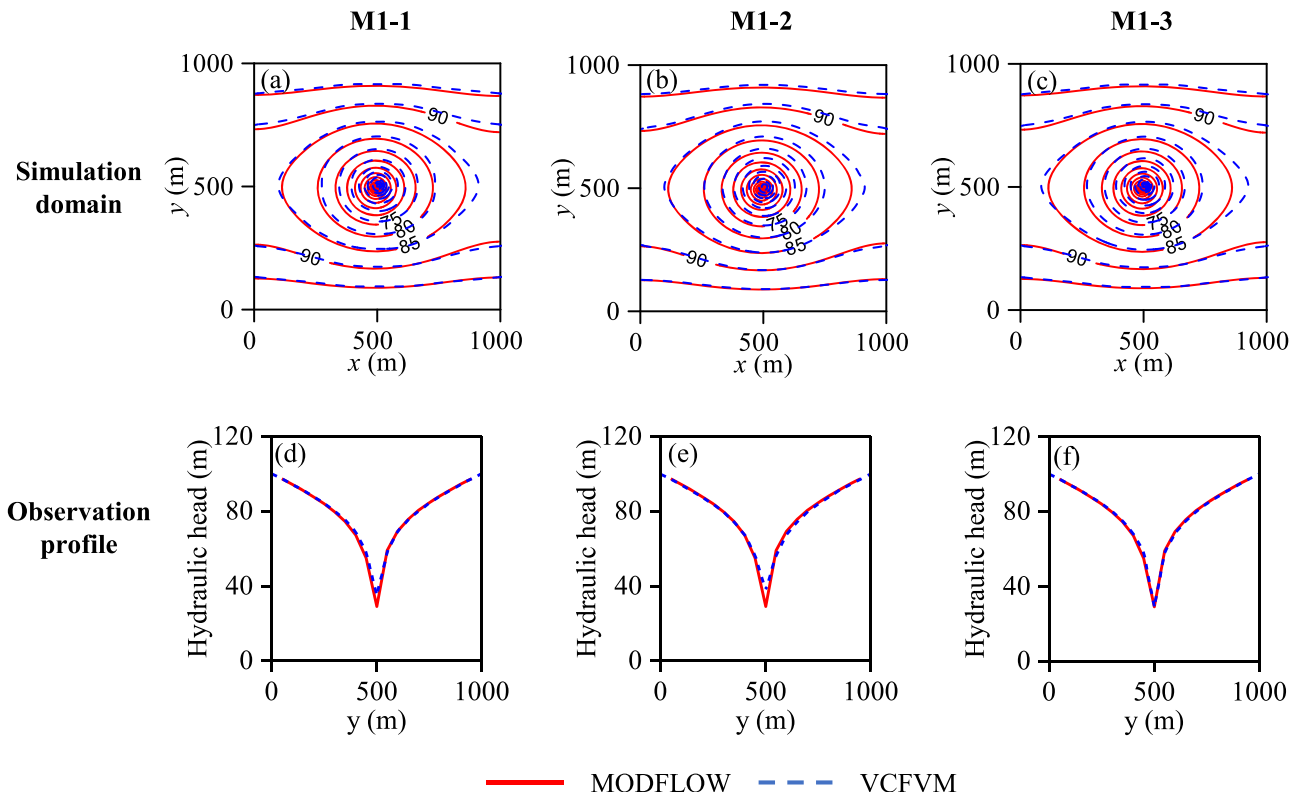


**Fig. 8.** Hydraulic heads in the simulation domain at 20 d of case 1 calculated by VCFVM using meshes with different shapes, (a) M1-1, (b) M1-2, (c) M1-3, and the corresponding hydraulic heads in observation profile, (d) M1-1, (e) M1-2, (f) M1-3, compared with MODFLOW.

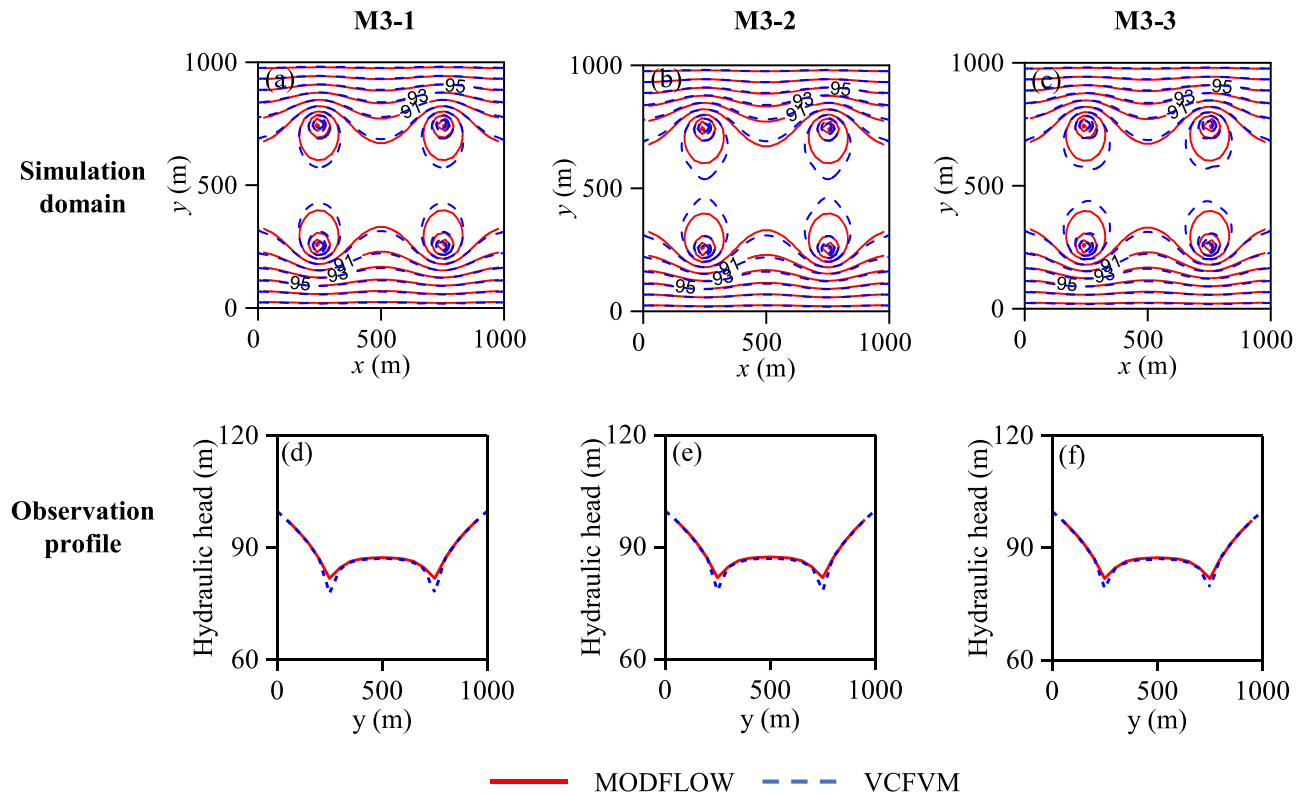


**Fig. 9.** Hydraulic heads in the simulation domain at 20 d of case 3 calculated by VCFVM using meshes with different shapes, (a) M3-1, (b) M3-2, (c) M3-3, and the corresponding hydraulic heads in observation profile, (d) M3-1, (e) M3-2, (f) M3-3, compared with MODFLOW.

**Table 6**  
Hydraulic head of each observation point and values of evaluation indices of cases 1-3.

Case number	Mesh scheme	Observation point number								MAE (m)	RRMSE (%)
		1	2	3	4	5	6	7	8		
Case 1	MODFLOW	87.82	83.93	88.20	80.42	81.22	88.09	84.56	88.44	/	/
	M1-1	87.83	84.38	87.83	81.11	81.11	87.83	84.38	87.83	0.34	0.48
	M1-2 (VCFVM)	87.89	83.74	87.89	80.26	80.26	87.89	83.74	87.89	0.33	0.43
	M1-2 (MODFLOW 6)	88.02	83.78	87.63	80.36	79.35	87.70	82.85	87.31	0.76	1.19
	M1-3	87.87	84.24	87.86	80.78	80.78	87.85	84.22	87.85	0.41	0.61
	M1-4 (VCFVM)	87.92	83.71	87.92	80.19	80.19	87.92	83.71	87.92	0.42	0.63
	M1-4 (MODFLOW 6)	88.29	84.87	87.93	79.90	78.95	87.42	82.06	87.06	1.13	1.61
	M1-5 (VCFVM)	87.60	83.68	87.60	80.04	80.04	87.60	83.68	87.60	0.61	0.81
	M1-5 (MODFLOW 6)	88.14	83.56	87.73	79.91	78.67	87.87	82.60	87.44	0.93	1.44
	M1-6 (VCFVM)	87.17	84.47	87.17	80.87	80.87	87.17	84.47	87.17	0.66	0.89
Case 2	M1-6 (MODFLOW 6)	87.30	82.41	86.59	78.43	76.93	86.76	81.24	86.19	2.10	2.79
	MODFLOW	88.50	87.98	88.55	87.50	87.61	88.54	88.06	88.59	/	/
	M2-1	88.53	88.11	88.53	87.71	87.71	88.53	88.11	88.53	0.07	0.11
	M2-2	88.54	88.02	88.51	87.60	87.55	88.54	88.02	88.51	0.05	0.07
Case 3	M2-3	88.56	88.11	88.55	87.70	87.69	88.56	88.11	88.55	0.07	0.11
	MODFLOW	93.92	92.92	93.97	88.97	89.07	87.76	86.78	87.82	/	/
	M3-1	93.85	92.89	93.85	88.87	88.87	87.58	86.55	87.60	0.14	0.18
	M3-2	93.80	92.82	93.80	88.75	88.75	87.50	86.41	87.51	0.23	0.28
	M3-3	93.73	92.83	93.77	88.89	88.80	87.50	86.46	87.42	0.23	0.28

Note: Without special instruction, the hydraulic heads and evaluation indices are those of the VCFVM.

The VCFVM using the different mesh schemes illustrated in Fig. 4(b)-(d) for case 1 are shown in Fig. 8, and the results for case 3 using the mesh schemes illustrated in Fig. 5(b)-(d) are shown in Fig. 9. The observation profile used in case 3 located at  $x=250$  m. The corresponding values of the evaluation indices are given in Table 5. For case 1, Fig. 8 shows that the hydraulic heads in the simulation domain and observation profile obtained by the VCFVM using the meshes of different shapes are consistent with those produced by MODFLOW. As shown in Table 6, the MAEs for the different mesh schemes in case 1 are 0.34 m, 0.33 m and 0.41 m, and the corresponding RRMSEs are 0.48%, 0.43% and 0.61%.

The discrepancies between the results obtained by MODFLOW and the VCFVM using meshes with different kinds of shapes are within acceptable range. For case 3, Fig. 9 shows that the hydraulic heads in the simulation domain and observation profile obtained by the VCFVM using the meshes of different shapes are consistent with those produced by MODFLOW. As shown in Table 6, the MAEs for different kinds of meshes in case 3 are smaller than 0.23 m, and the corresponding RRMSEs are smaller than 0.28%. The results of case 1 and case 3 demonstrate the accuracy of the VCFVM in confined aquifer problems using meshes with different shapes.

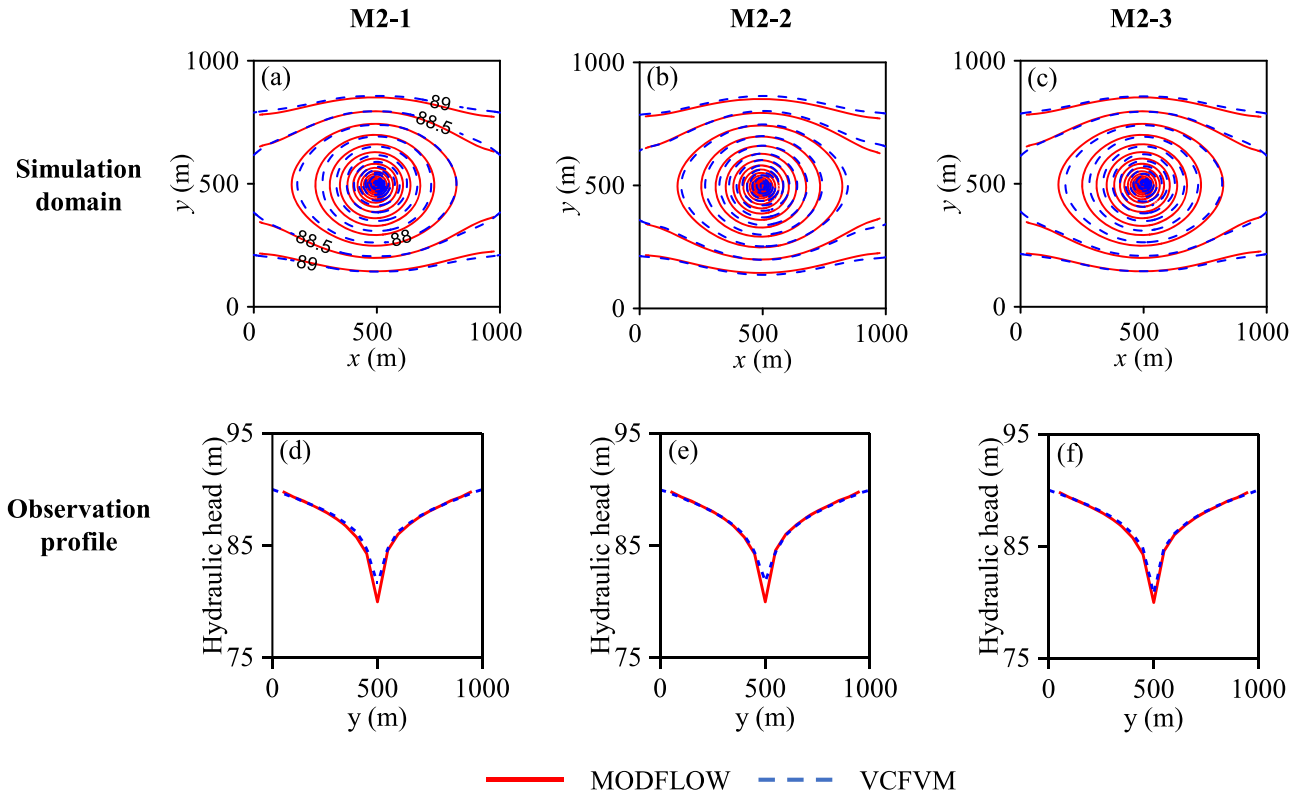


**Fig. 10.** Hydraulic heads in the simulation domain at 20 d of case 2 calculated by VCFVM using meshes with different shapes, (a) M2-1, (b) M2-2, (c) M2-3, and the corresponding hydraulic heads in observation profile, (d) M2-1, (e) M2-2, (f) M2-3, compared with MODFLOW.

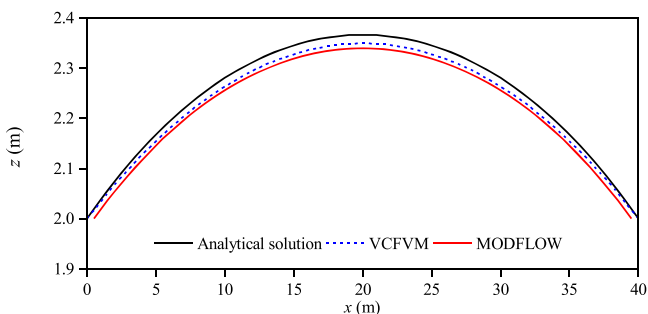


**Fig. 11.** Hydraulic head at 100 d of case 5 calculated by the VCFVM and MODFLOW compared with the analytical solution.

The hydraulic heads at 20 d in the simulation domain, and in the observation profile, located at  $x=500$  m, calculated by MODFLOW and the VCFVM using different mesh schemes illustrated in Fig. 4(b)-(d) for case 2 are shown in Fig. 10. The corresponding hydraulic heads at the eight observation points and the values of the evaluation indices are given in Table 6. The MAEs for different mesh schemes in case 2 are 0.07 m, 0.05 m and 0.07 m, and the corresponding RRMSEs are 0.11%, 0.07% and 0.11%, which demonstrate the accuracy of the VCFVM in unconfined aquifer cases.

To assess the accuracy of the VCFVM in dealing with the nonpoint source/sink terms, an analytical solution is obtained for case 4. When the groundwater reaches a steady state, the relationship between the groundwater level and the distance to the left canal can be expressed as follows:

$$H(x)^2 = (H_1)^2 + \frac{(H_2)^2 - (H_1)^2}{l} x + \frac{P}{K} \times (lx - x^2) \quad (43)$$

where  $l$  is the distance between the two canals, [L] and  $H_1$  and  $H_2$  are the

water levels in the left and right canals, respectively [L].

The groundwater level at steady state obtained by the VCFVM is compared to the analytical solution and the results of MODFLOW, as shown in Fig. 11. Notably, the VCFVM-simulated values are slightly lower than those based on the analytical solution and higher than those of MODFLOW, but all values are close to each other. The MAE values between the VCFVM result and the analytical solution, the VCFVM result and MODFLOW result, are both 0.01 m, indicating that the VCFVM can effectively deal with nonpoint source/sink terms.

According to the results above, the VCFVM has a second-order spatial accuracy, and can be accurately applied to problems involving confined aquifers, unconfined aquifers, heterogeneous and anisotropic aquifers, and nonpoint source/sink terms, which account for the majority of problems considered in conventional groundwater simulation.

#### 4.2. Ability of the VCFVM in dealing with nonmatching grids with different refinement ratios

The ability to deal with nonmatching grids, especially those with high refinement ratios, is one of the main advantages of the VCFVM. To demonstrate this, the accuracy of the VCFVM for scenarios involving nonmatching grids with different refinement ratios is demonstrated by simulating case 1 using meshes M1-2, M1-4, M1-5 and M1-6. The results obtained by MODFLOW using refined grids are used as benchmark. The results of the VCFVM and MODFLOW 6 using the same meshes are compared with those from MODFLOW. The comparison results of hydraulic heads at 20 d in observation profile located at  $x=500$  m simulated by MODFLOW, the VCFVM and MODFLOW 6, and also the discrepancies between results obtained by VCFVM or MODFLOW 6 and MODFLOW in the domain are shown in Fig. 12. The corresponding hydraulic heads at the eight observation points and the values of the evaluation indices are given in Table 6.

It can be found that the deviations between the results of VCFVM or MODFLOW 6 and MODFLOW increase with the larger refinement ratio

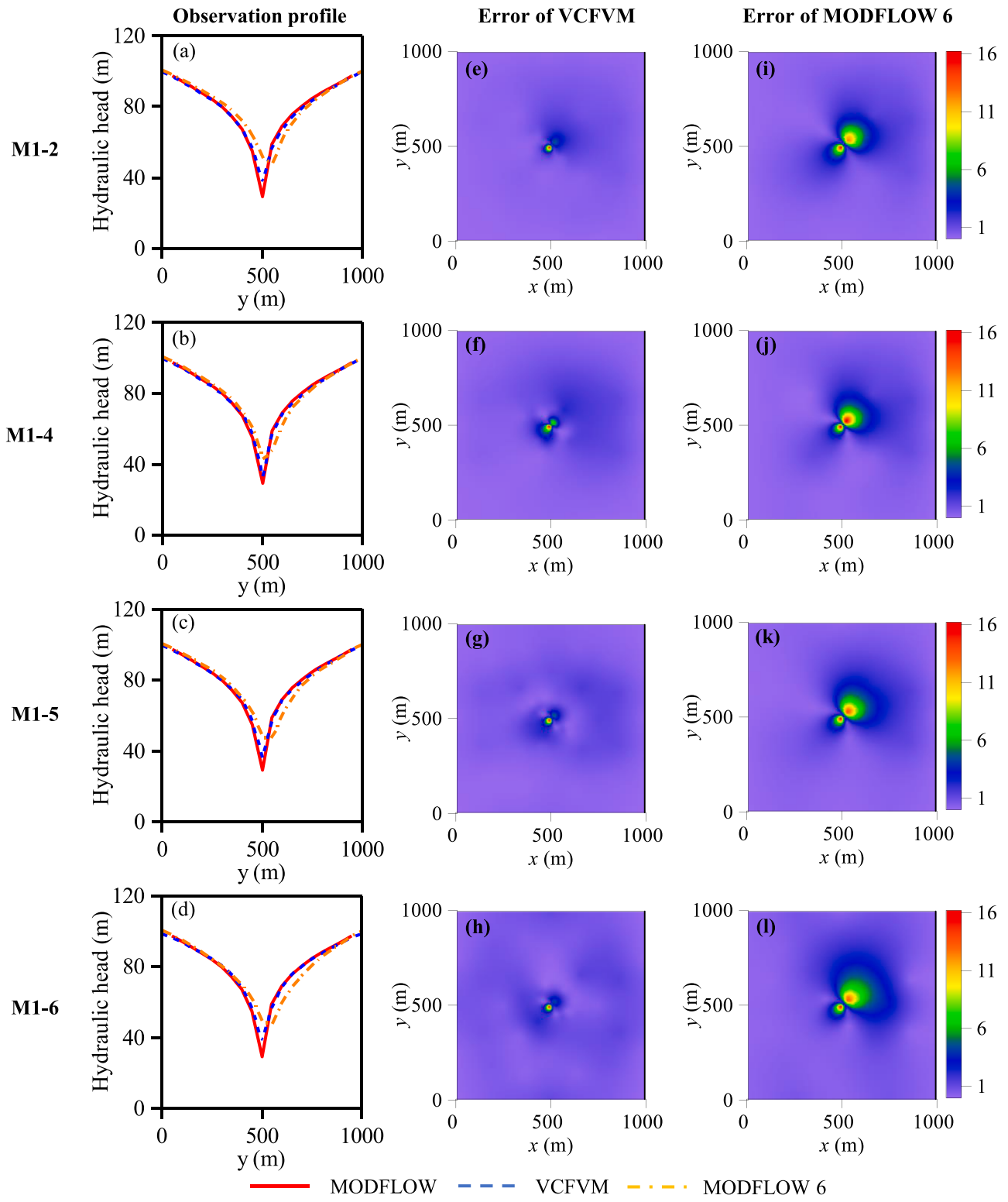


**Fig. 12.** Hydraulic heads at 20 d of test case 1 in observation profile obtained by the VCFVM or MODFLOW 6 using nonmatching grids compared with that obtained by MODFLOW (used as benchmark), (a) M1-2, (b) M1-4, (c) M1-5, (d) M1-6, and the corresponding discrepancies between VCFVM, (e)-(h), or MODFLOW 6, (i)-(l), with MODFLOW in the simulation domain.

as shown in Fig. 12 (a)-(d). The discrepancies between the VCFVM and MODFLOW are always lower than those between MODFLOW 6 and MODFLOW, as shown in the Fig. 12(e)-(l). In particular, the hydraulic heads obtained by MODFLOW 6 using the M1-6 mesh exhibit a large difference compared to those of MODFLOW, as shown in Fig. 12(l). Table 6 shows that the MAEs of the VCFVM range from 0.33 to 0.66 m,

and the MAEs of MODFLOW 6 range from 0.76 to 2.10 m. Additionally, the RRMSEs of VCFVM range from 0.43% to 0.89%, and those for MODFLOW 6 range from 1.19% to 2.79%. When the mesh with a refinement ratio of 1:6 (M1-6) is used, the error of MODFLOW 6 is nearly twice that of other meshes and is three times greater than the error of the VCFVM. It can be concluded that the VCFVM yields higher accuracy in

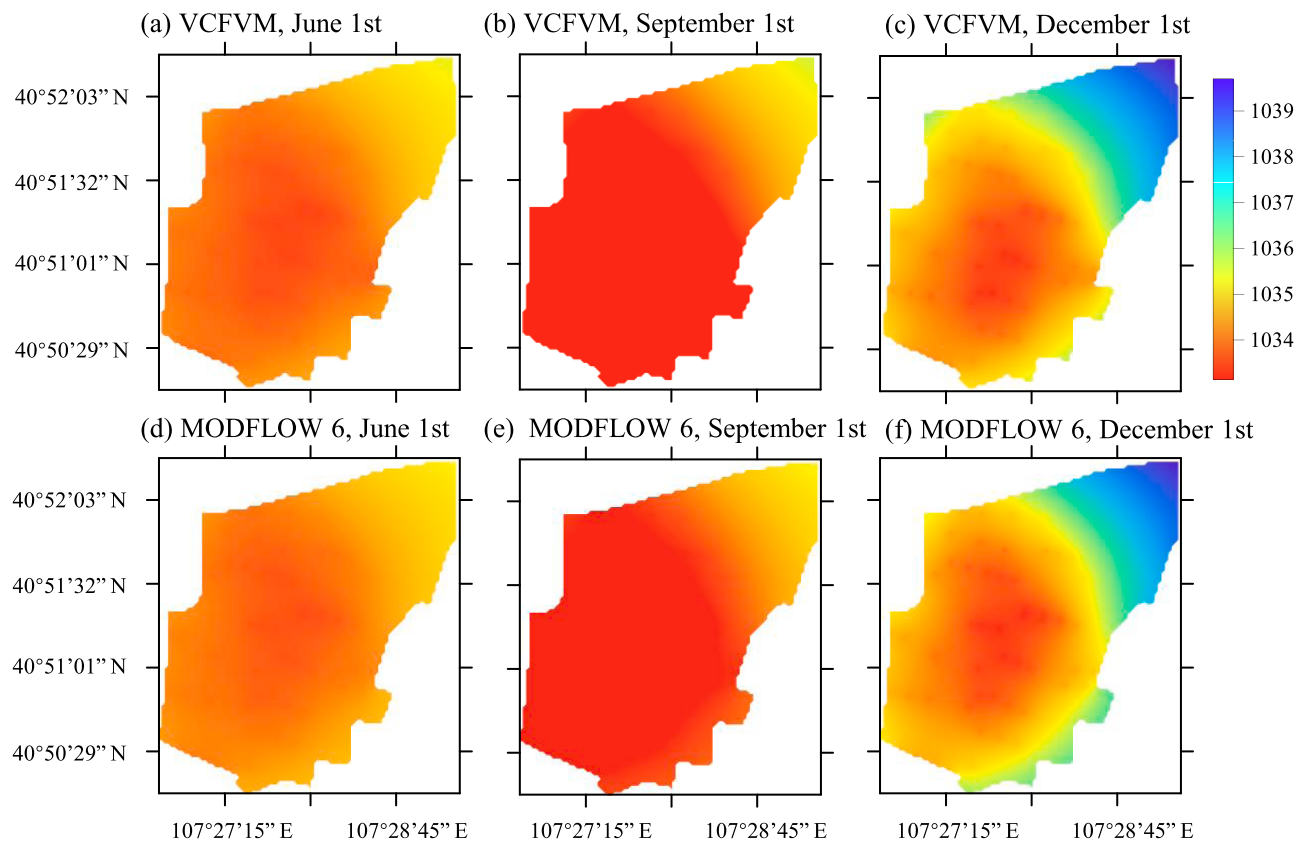


**Fig. 13.** Simulated Groundwater levels of test case 5 by the VCFVM and MODFLOW 6 in the simulation domain at different time stamps.

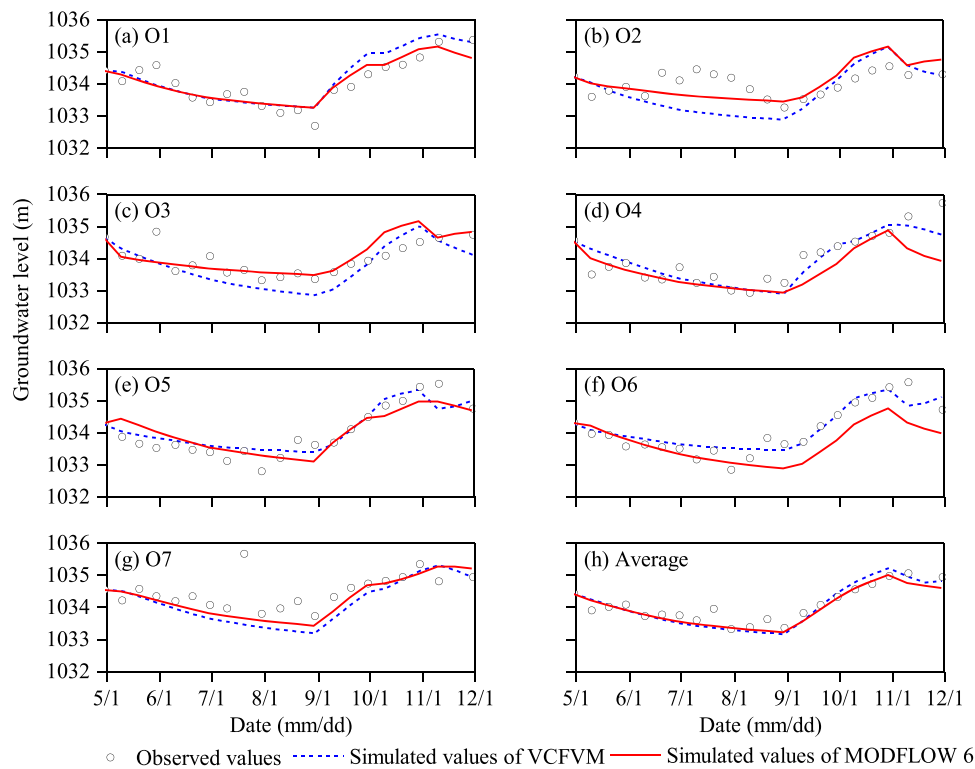


**Fig. 14.** Comparison of observed groundwater levels at observation wells along time with those simulated by the VCFVM and MODFLOW 6 of test case 5.

**Table 7**

Values of evaluation indices at each observation well of case 5.

Observation wells	MODFLOW 6		VCFVM	
	MAE (m)	RRMSE (%)	MAE (m)	RRMSE (%)
Ob1	0.25	8.23	0.34	11.21
Ob2	0.39	12.46	0.51	17.20
Ob3	0.25	10.06	0.37	11.83
Ob4	0.39	15.45	0.27	9.74
Ob5	0.30	10.00	0.25	8.46
Ob6	0.47	15.80	0.23	8.32
Ob7	0.36	16.86	0.45	19.90
Average values	0.35	12.69	0.35	12.38

**Table 8**The CPU time and  $E_B$  of cases 1 and 5 with different mesh schemes.

Test number	Mesh number	CPU time (s)	$E_B$ (%)
Case 1	MODFLOW	7.02	0.02
	M1-2	2.04	0.00
	MODFLOW 6	2.71	0.00
	M1-4	1.91	0.00
	MODFLOW 6	2.25	0.00
	M1-5	1.55	0.00
	MODFLOW 6	2.17	0.00
	M1-6	1.76	0.00
	MODFLOW 6	1.91	0.00
	VCFVM	1550	0.02
Case 5	MODFLOW 6	1563	0.03
	VCFVM	1563	0.03

cases with nonmatching grids, especially when the refinement ratio is high. In other words, the VCFVM exhibits very high accuracy for those control volumes with convex angles.

#### 4.3. Performance of the VCFVM in a real-world case

The accuracy of the VCFVM in a real-world case with multiple pumping wells is demonstrated by test case 5. The simulated groundwater levels of the VCFVM and MODFLOW 6 in simulation domain on June 1st, September 1st and December 1st are shown in Fig. 13, and the simulated and observed groundwater levels along time at each observation well, as well as the averaged groundwater level among all observation wells, are shown in Fig. 14. The corresponding evaluation indices are given in Table 7. It should be noted that the groundwater table depth, instead of the groundwater level, is used here to obtain the RRMSEs of the VCFVM and MODFLOW 6. As shown in Fig. 13, as expected, the groundwater level in the simulated domain gets deeper from June to September due to the water pumping for irrigation, and get recovered from September to December due to lateral recharge from adjacent areas with autumn irrigation. Moreover, the simulated groundwater levels in the domain obtained by the VCFVM are consistent with those of MODFLOW 6 at corresponding time. According to Fig. 14, slight differences between the results from the VCFVM and MODFLOW 6 are observed in single-well observations, as shown in Fig. 14(a)-(g), while the average values of the VCFVM are close to those of MODFLOW 6, as shown in Fig. 14(h), and both sets of results from the VCFVM and MODFLOW 6 are similar to the observed values. As shown in Table 7, the MAEs of the VCFVM range from 0.25 to 0.51 m at different observation wells, and the values of MODFLOW 6 range from 0.25 to 0.47 m. The average values of MAE for both the VCFVM and MODFLOW 6 are 0.35 m. The RRMSEs of the VCFVM at different observation wells range from 8.32% to 19.90%, with an average value of 12.38%, and those of MODFLOW 6 range from 8.23% to 16.86%, with an average value of 12.69%. It can be concluded from this case that the VCFVM has good performance under complex practical conditions, as indicated by comparing the simulation results to results from MODFLOW 6 and the observed data.

#### 4.4. Efficiency of the VCFVM in dealing with LGR meshes

The computational efficiency of the VCFVM was compared with the efficiency of MODFLOW/MODFLOW 6 using the results from case 1 and case 5. The CPU time and  $E_B$  for case 1 and case 5 using different mesh schemes are given in Table 8.

For case 1, the total CPU time for MODFLOW is 7.02 s, and it takes 2.04 s, 1.91 s, 1.55 s and 1.76 s for the VCFVM to run in the four mesh schemes (M1-2, M1-4, M1-5 and M1-6, respectively) and 2.71 s, 2.25 s, 2.17 s and 1.91 s for MODFLOW 6 with the corresponding schemes. The  $E_B$  of MODFLOW is 0.021 %, and it is nearly 0.000 % for both the VCFVM and MODFLOW 6 for all mesh schemes. For test case 5, the total CPU time of the VCFVM and MODFLOW 6 are 1563 s and 1550 s for the same mesh scheme, respectively. The  $E_B$  of the VCFVM is 0.03%, and that of MODFLOW 6 is 0.02 %. It can be concluded that both the VCFVM and MODFLOW 6 have advantages in saving computational time and conserving the mass balance. The CPU time of MODFLOW 6 is slightly shorter than that of the VCFVM in test case 5, mainly because the advanced linearization scheme, specifically, the Newton-Raphson method (Langevin et al., 2017), is adopted to deal with unconfined aquifer conditions, which can be further improved in our developed model.

#### 5. Conclusions

In this paper, a numerical groundwater model based on the VCFVM is proposed. All unknowns to be solved are associated with vertices, and the control volume could be defined for each vertex, including the nonmatching vertices. Then, the hydraulic head in the whole simulation area can be obtained by solving the matrix equations without additional treatment at the nonmatching vertices. The accuracy and performance of the algorithm were tested based on several cases, and the major conclusions can be made as follows.

- (1) The VCFVM can obtain accurate hydraulic heads with negligible mass balance errors using different arbitrary polygonal grids in confined and unconfined aquifers involving heterogeneous anisotropic transmissivities and nonpoint source/sink terms.
- (2) The VCFVM can simulate groundwater problems using meshes with high refinement ratios with high accuracy.
- (3) The VCFVM exhibits high efficiency in dealing with nonmatching grids with high refinement ratios and performs well in mass balance due to local conservation of the numerical flux.
- (4) The current version of VCFVM is a 2-D model, and the extension of the model to 3-D must be further studied. Since a simple linearization scheme is used by the VCFVM to solve unconfined aquifer problems, the adoption of more efficient methods, such as the Newton-Raphson method, remains to be further explored.

#### CRediT authorship contribution statement

**Yingzhi Qian:** Validation, Writing – original draft. **Yan Zhu:** Conceptualization, Methodology, Writing – review & editing. **Xiaoping Zhang:** Conceptualization, Methodology, Writing – review & editing. **Jiming Wu:** Methodology. **Ming Ye:** Writing – review & editing. **Wei Mao:** Writing – review & editing. **Jingwei Wu:** Funding acquisition. **Jiesheng Huang:** Funding acquisition, Supervision. **Jinzhong Yang:** Writing – review & editing.

#### Declaration of Competing Interest

The authors declare that they have no known competing financial interests or personal relationships that could have appeared to influence the work reported in this paper.

## Data availability

Data will be made available on request.

## Acknowledgements

The study was partially supported by the National Key Research and Development Program of China (2021YFD1900805-02), and National Natural Science Foundation of China through Grants 51790533, 52179041. Yingzhi Qian was sponsored the China Scholarship Council (No. 202106270106).

## Supplementary materials

Supplementary material associated with this article can be found, in the online version, at doi:[10.1016/j.advwatres.2023.104392](https://doi.org/10.1016/j.advwatres.2023.104392).

## References

- Abdulle, A., E, W., 2003. Finite difference heterogeneous multi-scale method for homogenization problems. *J. Comput. Phys.* 191 (1), 18–39. [https://doi.org/10.1016/S0021-9991\(03\)00303-6](https://doi.org/10.1016/S0021-9991(03)00303-6).
- Arbogast, T., Cowsar, L.C., Yotov, W.I., 2000. Mixed finite element methods on nonmatching multiblock grids. *SIAM J. Numer. Anal.* 37 (4), 1295–1315. <https://doi.org/10.1137/S0036142996308447>.
- Borsi, I., Rossetto, R., Schifani, C., Hill, M.C., 2013. Modeling unsaturated zone flow and runoff processes by integrating MODFLOW-LGR and VSF, and creating the new CFL Package. *J. Hydrol.* 488, 33–47. <https://doi.org/10.1016/j.jhydrol.2013.02.020>.
- Brunner, P., Simmons, C.T., 2012. HydroGeoSphere: a fully integrated, physically based hydrological model. *Groundwater* 50 (2). <https://doi.org/10.1111/j.1745-6584.2011.00882.x>.
- Chen, F., Ren, L., 2014. New scheme of finite difference heterogeneous multiscale method to solve saturated flow in porous media. *Abstr. Appl. Anal.* 575298, 1–19. <https://doi.org/10.1155/2014/575298>. Article ID2014.
- Chen, Z.M., Hou, T.Y., 2003. A mixed multiscale finite element method for elliptic problems with oscillating coefficients. *Math. Comput.* 72 (242), 541–576. <https://doi.org/10.1090/S0025-5718-02-01441-2>.
- Chung, E.T., Efendiev, Y., Lee, C.S., 2015. Mixed generalized multiscale finite element methods and applications. *Multiscale Model. Simul.* 13 (1), 338–366. <https://doi.org/10.1137/140970574>.
- Dickinson, J.E., James, S.C., Mehl, S., Hill, M.C., Leake, S.A., Zyvoloski, G.A., Faunt, C.C., Eddebbarh, A.A., 2007. A new ghost-node method for linking different models and initial investigations of heterogeneity and nonmatching grids. *Adv. Water Resour.* 30, 1722–1736. <https://doi.org/10.1016/j.advwatres.2007.01.004>.
- Diersch, H.-J.G., 1998. FEFLOW Reference manual. WASY, Berlin, Germany, p. 278. Institute of Water Resources Planning and System Research Ltd.
- Domelevo, K., Omnes, P., 2005. A finite volume method for the Laplace equation on almost arbitrary two-dimensional grids. *M2AN Math. Model. Numer. Anal.* 39 (6) <https://doi.org/10.1051/m2an:2005047>.
- Durlofsky, L.J., Efendiev, Y., Ginting, V., 2007. An adaptive local-global multiscale finite volume element method for two-phase flow simulations. *Adv. Water Resour.* 30 (3), 576–588. <https://doi.org/10.1016/j.advwatres.2006.04.002>.
- Ewing, R.E., Wang, J.P., 1992. Analysis of mixed finite element methods on locally refined grids. *Numer. Math.* 63 (1), 183–194. <https://doi.org/10.1007/BF01385855>.
- Edwards, M.G., 2006a. Higher-resolution hyperbolic-coupled-elliptic flux-continuous CVD schemes on structured and unstructured grids in 2-D. *Int. J. Numer. Meth. Fluids* 51, 1059–1077. <https://doi.org/10.1002/fld.1245>.
- Edwards, M.G., 2006b. Higher-resolution hyperbolic-coupled-elliptic flux-continuous CVD schemes on structured and unstructured grids in 3-D. *Int. J. Numer. Meth. Fluids* 51, 1079–1095. <https://doi.org/10.1002/fld.1289>.
- Edwards, M.G., Zheng, H., 2010. Double-families of Quasi-Positive Darcy-Flux Approximations with Highly Anisotropic Tensors on Structured and Unstructured Grids. *J. Comput. Phys.* 229, 594–625. <https://doi.org/10.1016/j.jcp.2009.09.037>, 2010.
- Feinstein, D.T., Fienen, M.N., Reeves, H.W., Langevin, C.D., 2016. A Semi-Structured MODFLOW-USG Model to Evaluate Local Water Sources to Wells for Decision Support. *Groundwater* 54, 532–544. <https://doi.org/10.1111/gwat.12389>.
- Fu, S., Chung, E., 2019. A local-global multiscale mortar mixed finite element method for multiphase transport in heterogeneous media. *J. Comput. Phys.* 399, 108906 <https://doi.org/10.1016/j.jcp.2019.108906>, 2019.
- Ganis, B., Wheeler, M.F., Yotov, I., 2015. An Enhanced Velocity multipoint Flux Mixed Finite Element Method for Darcy Flow on Non-matching Hexahedral Grids. *Procedia Comput. Sci.* 51, 1198–1207. <https://doi.org/10.1016/j.procs.2015.05.295>.
- Gao, Y., Li, Y., 2017. A mortar mixed finite volume method for elliptic problems on non-matching multi-block triangular grids. *J. Sci. Comput.* 72, 50–69. <https://doi.org/10.1007/s10915-017-0405-z>.
- Guwanasen, V., East, S., Floor, T., Guwanasen, V., and Inc, H.: FRAC3DVS-OPG Enhancements: subgridding, hydromechanical deformation and anisotropic molecular diffusion. Nuclear Waste Management Organization Report NWMO-TR-2007-05, 2007.
- Hajibeygi, H., Bonfigli, G., Hesse, M.A., Jenny, P., 2008. Iterative multiscale finite-volume method. *J. Comput. Phys.* 227, 8604–8621. <https://doi.org/10.1016/j.jcp.2008.06.013>, 2008.
- Harbaugh, A.W., Banta, E.R., Hill, M.C., and McDonald, M.G.: MODFLOW-2000, The US Geological Survey modular ground-water model—User guide to modularization concepts and the ground-water flow process, US Geological Survey Open-File Report 00-92, 2000.
- He, X., Ren, L., 2005. Finite volume multiscale finite element method for solving the groundwater flow problems in heterogeneous porous media. *Water Resour. Res.* 41 (10), 10417. <https://doi.org/10.1029/2004WR003934>.
- He, X., Ren, L., 2006. A modified multiscale finite element method for well-driven flow problems in heterogeneous porous media. *J. Hydrol.* 329 (3-4), 674–684. <https://doi.org/10.1016/j.jhydrol.2006.03.018>.
- Herckenrath, D., Doherty, J., Panday, S., 2015. Incorporating the effect of gas in modelling the impact of CBM extraction on regional groundwater systems. *J. Hydrol.* 523, 587–601. <https://doi.org/10.1016/j.jhydrol.2015.02.012>.
- Hou, T.Y., Wu, X.H., 1997. A multiscale finite element method for elliptic problems in composite materials and porous media. *J. Comput. Phys.* 134 (1), 169–189. <https://doi.org/10.1006/jcph.1997.5682>.
- Jenny, P., Lee, S.H., Tchelepi, H.A., 2003. Multi-scale finite-volume method for elliptic problems in subsurface flow simulation. *J. Comput. Phys.* 187 (1), 47–67. [https://doi.org/10.1016/S0021-9991\(03\)00075-5](https://doi.org/10.1016/S0021-9991(03)00075-5).
- Jenny, P., Lunati, I., 2009. Modeling complex wells with the multi-scale finite-volume method. *J. Comput. Phys.* 228 (3), 687–702. <https://doi.org/10.1016/j.jcp.2008.09.026>.
- Kramarenko, V., Nikitin, K., Vassilevski, Y., 2017. A finite volume scheme with improved well modeling in subsurface flow simulation. *Comput. Geosci.* 21 (5-6), 1–11. <https://doi.org/10.1007/s10596-017-9685-5>.
- Krcmar, D., Sracek, O., 2014. MODFLOW-USG: the New Possibilities in Mine Hydrogeology Modelling (or What is Not Written in the Manuals). *Mine Water Environ.* 33, 376–383. <https://doi.org/10.1007/s10230-014-0273-9>.
- Langevin, C.D., Hughes, J.D., Banta, E.R., Provost, A.M., Niswonger, R.G., Panday, Sorab, 2017. MODFLOW 6 Modular Hydrologic Model. U.S. Geological Survey Software. doi:0.5066/F76Q1VQV.
- Lien, J., Liu, G., and Langevin, C.D.: GRIDGEN version 1.0 – A computer program for generating unstructured finite-volume grids: U.S. Geological Survey Open-File Report 2014-1109, 39 p., doi: 10.3133/ofr20141109, 2015.
- Lunati, I., Tyagi, M., Lee, S.H., 2011. An iterative multiscale finite volume algorithm converging to the exact solution. *J. Comput. Phys.* 230 (5), 1849–1864. <https://doi.org/10.1016/j.jcp.2010.11.036>.
- Manzoor, S., Edwards, M.G., Dogru, A.H., 2021. Three-dimensional unstructured gridding for complex wells and geological features in subsurface reservoirs, with CVD-MPFA discretization performance. *Comput. Meth. Appl. Mech. Eng.* 373, 113389 <https://doi.org/10.1016/j.cma.2020.113389>, 2021.
- Matous, K., Geers, M.G.D., Kouznetsova, V.G., Gillman, A., 2017. A review of predictive nonlinear theories for multiscale modelling of heterogeneous materials. *J. Comput. Phys.* 330, 192–220. <https://doi.org/10.1016/j.jcp.2016.10.070>, 2016.
- Matthäi, S.K., Mezentsev, A.A., Pain, C.C., Eaton, M.D., 2005. A high-order TVD transport method for hybrid meshes on complex geological geometry. *Int. J. Numer. Meth. Fluids* 47, 1181–1187. <https://doi.org/10.1002/fld.901>.
- Matthai, S.K., Mezentsev, A., Belayneh, M., 2007. Finite element-node-centered finite-volume two-phase-flow experiments with fractured rock represented by unstructured hybrid-element meshes. *SPE Reserv. Eval. Eng.* 10 (06), 740–756. <https://doi.org/10.2118/93341-PA>.
- Mehl, S., Hill, M.C., 2002. Development and evaluation of a local grid refinement method for block-centered finite-difference groundwater models using shared nodes. *Adv. Water Resour.* 25, 497–511. [https://doi.org/10.1016/S0309-1708\(02\)00021-0](https://doi.org/10.1016/S0309-1708(02)00021-0).
- Panday, S., Langevin, C.D., 2012. Improving sub-grid scale accuracy of boundary features in regional finite-difference models. *Adv. Water Resour.* 41, 65–75. <https://doi.org/10.1016/j.advwatres.2012.02.011>.
- Panday, S., Langevin, C.D., Niswonger, R.G., Ibaraki, Motomu, and Hughes, J.D.: MODFLOW-USG version 1: An unstructured grid version of MODFLOW for simulating groundwater flow and tightly coupled processes using a control volume finite-difference formulation: U.S. Geological Survey Techniques and Methods, book 6, chap. A45, 66 p., <https://www.usgs.gov/software/modflow-usg-unstructured-grid-version-modflow-simulating-groundwater-flow-and-tightly>, 2013.
- Romero, D.M., Silver, S.E., 2006. Grid cell distortion and modflow's integrated finite-difference numerical solution. *Groundwater* 44 (6), 797–802. <https://doi.org/10.1111/j.1745-6584.2005.00179.x>.
- Saad, Y., 2003. Iterative Methods for Sparse Linear Systems. Siam 151–216. <https://doi.org/10.1137/1.9780989718003.ch6>.
- Székely, F., 1998. Windowed spatial zooming in finite-difference ground water flow models. *Groundwater* 36, 718–721. <https://doi.org/10.1111/j.1745-6584.1998.tb02188.x>.
- Therrien, R., Sudicky, E.A., 1996. Three-dimensional analysis of variably-saturated flow and solute transport in discretely-fractured porous media. *J. Contam. Hydrol.* 23 (1–2), 1–44. [https://doi.org/10.1016/0169-7722\(95\)00088-7](https://doi.org/10.1016/0169-7722(95)00088-7).
- Thomas, S.G., Wheeler, M.F., 2011. Enhanced velocity mixed finite element methods for modeling coupled flow and transport on non-matching multiblock grids. *Comput. Geosci.* 15 (4), 605–625. <https://doi.org/10.1007/s10596-011-9227-5>.
- Trefry, M.G., Muffels, C., 2007. FEFLOW: A finite-element groundwater flow and transport modeling tool. *Groundwater* 45 (5), 525–528. <https://doi.org/10.1111/j.1745-6584.2007.00358.x>.

- Vilhelmsen, T.N., Christensen, S., Mehl, S.W., 2011. Evaluation of MODFLOW-LGR in connection with a synthetic regional-scale model. *Groundwater* 50, 118–132. <https://doi.org/10.1111/j.1745-6584.2011.00826.x>.
- Ward, D.S., Buss, D.R., Mercer, J.W., Hughes, S.S., 1987. Evaluation of a groundwater corrective action at the Chem-Dyne Hazardous Waste Site using a telescopic mesh refinement modeling approach. *Water Resour. Res.* 23, 603–617. <https://doi.org/10.1029/WR023i004p00603>.
- Wen, X.H., Gómez-Hernández, J.J., 1996. Upscaling hydraulic conductivities in heterogeneous media: an overview. *J. Hydrol.* 183 (1-2), ix–xxxii. [https://doi.org/10.1016/S0022-1694\(96\)80030-8](https://doi.org/10.1016/S0022-1694(96)80030-8).
- Wheeler, J.A., Wheeler, M.F., Yotov, I., 2002. Enhanced velocity mixed finite element methods for flow in multiblock domains. *Comput. Geosci.* 6 (3-4), 315–332. <https://doi.org/10.1023/A:1021270509932>.
- Wolfsteiner, C., Lee, S.H., Tchelapi, H.A., 2006. Well modeling in the multiscale finite volume method for subsurface flow simulation. *Multiscale Model. Simul.* 5 (3), 900–917. <https://doi.org/10.1137/050640771>.
- Wu, J., 2017. Vertex-Centered Linearity-Preserving Schemes for Nonlinear Parabolic Problems on Polygonal Grids. *J Sci Comput* 71, 499–524. <https://doi.org/10.1007/s10915-016-0309-3>, 2017.
- Xie, Y., Wu, J., Xue, Y., Xie, C., 2016. Efficient triple-grid multiscale finite element method for solving groundwater flow problems in heterogeneous porous media. *Transp. Porous Media* 112, 361–380. <https://doi.org/10.1007/s11242-016-0650-x>.
- Xie, Y., Wu, J., Nan, T., Xue, Y., Xie, C., Ji, H., 2017. Efficient triple-grid multiscale finite element method for 3d groundwater flow simulation in heterogeneous porous media. *J. Hydrol.* 546, 503–514. <https://doi.org/10.1016/j.jhydrol.2017.01.027>.
- Xie, Y., Lu, C., Xue, Y., Ye, Y., Xie, C., Ji, H., Wu, J., 2019. New finite volume multiscale finite element model for simultaneously solving groundwater flow and darcian velocity fields in porous media. *J. Hydrol.* 573, 592–606. <https://doi.org/10.1016/j.jhydrol.2019.04.004>.
- Yang, Y., Zhu, Y., Mao, W., Dai, H., Ye, M., Wu, J., Yang, J., 2021. Study on the Exploitation Scheme of Groundwater under Well-Canal Conjunctive Irrigation in Seasonally Freezing-Thawing Agricultural Areas. *Water* 13, 1384. <https://doi.org/10.3390/w13101384>.
- Ye, S., Xue, Y., Xie, C., 2004. Application of the multiscale finite element method to flow in heterogeneous porous media. *Water Resour. Res.* 40, W09202. <https://doi.org/10.1029/2003WR002914>.
- Zhang, X., Su, S., Wu, J., 2017. A vertex-centered and positivity-preserving scheme for anisotropic diffusion problems on arbitrary polygonal grids. *J. Comput. Phys.* 344, 419–436. <https://doi.org/10.1016/j.jcp.2017.04.070>, 2017.